Study of variations of the dynamics of the Metal-Insulator transition of thin films of Vanadium Dioxide with an ultra-fast laser

Elizabeth Radue

Mount Airy, Maryland

Master of Science, College of William and Mary, 2011
Bachelor of Arts, Mount Holyoke College, 2009

A Dissertation presented to the Graduate Faculty
of the College of William and Mary in Candidacy for the Degree of
Doctor of Philosophy

Department of Physics

The College of William and Mary
May 2016

APPROVAL PAGE

This Dissertation is submitted in partial fulfillment of
the requirements for the degree of

Doctor of Philosophy

Elizabeth Radue

Approved by the Committee, June, 2016

Committee Chair
Associate Professor of Physics Irina Novikova, Physics
The College of William and Mary

Virginia Microelectronics Consortium Distinguished Professor of Physics R. A.

Lukaszew, Physics
The College of William and Mary

Associate Professor Enrico Rossi, Physics
The College of William and Mary

Associate Professor Mumtaz Quazilbash, Physics
The College of William and Mary

Dr. Russell A. Wincheski, Aerospace Technologist
NASA Langley Research Center

APPROVAL PAGE

This Dissertation is submitted in partial fulfillment of
the requirements for the degree of

Doctor of Philosophy

Elizabeth Radue

Draft Version, June 2016

Committee Chair
Associate Professor of Physics Irina Novikova, Physics
The College of William and Mary

Virginia Microelectronics Consortium Distinguished Professor of Physics R. A.

Lukaszew, Physics
The College of William and Mary

Associate Professor Enrico Rossi, Physics
The College of William and Mary

Associate Professor Mumtaz Quazilbash, Physics
The College of William and Mary

Dr. Russell A. Wincheski, Aerospace Technologist
NASA Langley Research Center

ABSTRACT

Vanadium dioxide is an intensely studied material, since it goes through an insulator-metal transition at a critical temperature just above room temperature at 340 K. The dramatic change in conductivity and the easily accessible transition temperature makes it an attractive material for novel technologies. Thin films of VO_2 have a reversible transition without any significant degradation in contrast, and depending on the microstructure of the films, the properties of the transition are tunable. In this work, I study the dynamics of the insulator-transition in thin films grown on different substrates using a pump-probe configuration. The energy needed to trigger the transition, as well as the time constants of the change in reflectivity are affected by the strain in the VO_2 films. I also characterized the samples using Raman spectroscopy and XRD measurements in order to identify what underlies the differences in behavior. Finally, in collaboration with Dr. Yamaguchi's group at RPI, I show that it is possible to trigger the transition using a THz pulse that directly pumps energy into the lattice, and at lower energies than needed to pump films by photoinducing the electrons across the band gap.

TABLE OF CONTENTS

CHAPTER

ACKNOWLEDGMENTS

I would like to thank my advisor Irina Novikova for all her guidance and support in this project. I would also like to thank Ale Lukaszew, both for the generous use of her lab and for her mentorship. I would like to thank Enrico Rossi for working with us on the theory, Buzz Wincheski for allowing us to use the facilities at NASA Langley, and Dr. Yamaguchi and his student Zhengping Fu for aiding us with the THz pump measurements at RPI. I would also like to thank all the students I worked with, particularly Matt Simons, Lei Wang, Martin Rodriguez-Vega, Eric Chrisman, Ashna Aggarwal, and Haley Bauser. Thanks also go to my fellow lab mates Gleb and Mi, for listening to me whine about temperamental lasers on a frequent basis.

I would also like to express my gratitude to all the excellent physics teachers that have gotten me this far, in particular to my undergraduate advisor Shubha Tewari. Thank you for all your encouragement and your continued support over the years. Finally, I would like to extend profound thanks to all my friends and family who have been my cheerleaders in the past 6 years. You kept me laughing and gave me the confidence I needed to see this through.

I present this thesis in honor of my parents, Peter and Nanette Radue.

LIST OF TABLES

LIST OF FIGURES

STUDY OF VARIATIONS OF THE DYNAMICS OF THE METAL-INSULATOR TRANSITION OF THIN FILMS OF VANADIUM DIOXIDE WITH AN ULTRA-FAST LASER

CHAPTER 1

Introduction

1.1 Overview of Dissertation

This dissertation describes my work with ultrafast studies of the insulator-metal transition in VO_2 thin films. I characterized the samples we received from UVA with cw measurements, Raman spectroscopy, and X-Ray diffraction (XRD). I measured the dynamics of an optically induced insulator-metal transition with an 800 nm ∼100 fs laser pulse in a pump-probe configuration, finding the dynamics to change from sample to sample.

1.2 Motivation for studying VO_2

One of the reason that VO_2 has had so much attention compared to other materials that display a insulator-metal transition is the fact that the transition happens right above room temperature at 340 K (68° C)[5, 6]. This is an easily accessible temperature for experimenters, who will always prefer a low hanging fruit. Other materials that have an insulator-metal transition have a T_c that is either accessible by a cryostat, like V_2O_3 which has a T_c at 150 K [7], or happens at a temperature that is too high to access, like NbO_2

which have a T_c at 1082 K [8]. This convenient T_c also makes VO_2 an attractive material to implement in new technologies. There is a large change in conductivity that can happen on a femtosecond timescale, faster than most electronic systems can respond. VO_2 could be used for ultrafast switches, in both electronic and plasmonic systems. It has also been proposed that it could be used for a coating for smart windows that would automatically change how much inferred radiation is reflected depending on the temperature, making buildings more energy efficient. There has been work to develop VO_2 as a thermal switch to cut of current when a system becomes too hot.

When using VO_2 in these applications, it's typically in the form of a nanocrystal or thin film. While bulk VO_2 cracks and deforms under the strain of the transition, nanoscale VO_2 can go through the insulator-metal transition Thin films also have reversible transitions, and the properties of the insulator-metal transition can be tuned by changing the strain and defects of the film.[9, 10, 11, 12, 13].We also find that films with different microstructures will have different dynamics when optically pumped, both in transitioning to the metallic state, and recovering back to the insulating state.

This work looks at VO_2 films grown on sapphire and rutile, which have very different strain, and how that effects the insulator-metal transition both thermally and optically induced.

1.3 Chapter Descriptions

In this work, I will first introduce the background on the current understanding of the insulator-metal transition in VO_2 in Chapter 22, including the previous work that has been done with ultrafast studies. In chapter 3 I will go over the characterization of our samples. This includes measurements done with continuous wave lasers while heating the films through the transition, dc-conductivity measurements with four-point probe, ellipsometry, and Raman spectroscopy measurements. I will also briefly go over my reflectivity and transmission calculations for thin films.

Chapter 4 will then describe the pump-probe experimental set-up, which is the primary experimental method used in this work. This will cover the laser system used, the characterization of the pulses, and the cryostat system used for cooling the samples. Chapter 5 discusses the work I did mapping out the response of the VO_2 thin films, varying the pump fluence and the initial temperature of the thin films. Then in Chapter **??** I show some interesting measurements looking at the sub-picosecond response in the films when I change the duration of the pump and probe pulse. The following chapter, Chapter 7 looks at the recovery times back to the insulating state once the films have been optically pumped. Finally, Chapter 8 will cover the experiments preformed at RPI with Dr. Yamaguchi's group, pumping with a broad-band THz pump, instead of an optical pump.

CHAPTER 2

Background on Insulator-Metal Transition in VO_2

2.1 Vanadium Dioxide

2.1.1 Phases of VO_2

Vanadium Dioxide is a highly correlated material that undergoes an insulator-metal transition when heated. At low temperatures the material is an insulator (or semiconductor), and when it is heated past 340 K the dc conductivity increases by five orders of magnitude. This is an easily accessible transition temperature, making VO_2 a popular material to study. In addition, the optical properties change as well, most dramatically in the infrared range.

VO_2 has four different phases currently known. At high temperatures, above a critical temperature T_c=340 K, Vanadium dioxide has a tetragonal/rutile lattice structure, with lattice constants of a_r=4.55 Åand c_r=2.85 Å. This is known as R-VO_2 and is the metallic phase. There is the room temperature M1 phase, where the lattice structure is monoclinic.

Below T_c the lattice breaks symmetry, and the Vanadium ions pair up and tilt off the c_r axis with the oxygen ions still in a octahedra around the V^{+4} ions. The monoclinic lattice constants are $a_m \approx 2c_r$, $b_m \approx a_r$, and $c_m \approx a_r - c_r$. ($a_m = 5.70$ $b_m = 4.55$ $c_m = 5.37$)[14] Figure 2.1 shows both the change in symmetry and shift in band structure in VO_2.

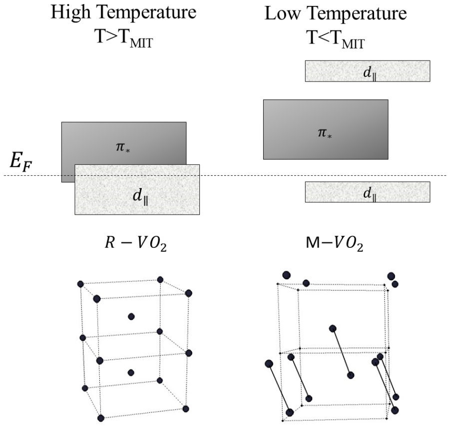

FIG. 2.1: Schematics of the VO_2 lattice structure and electron energy band structure below and above the critical MIT temperature. High-temperature metallic phase corresponds to the tetragonal (or rutile) lattice structure. During the thermally induced phase transition the V^{4+} ions dimerize along the c-axis of the tetragonal phase, breaking the symmetry and forming monoclinic lattice cells. At the same time the *d* band splits into two different bands, while the $\pi*$ band shifts above the Fermi level E_F, drastically decreasing electron conductivity.[1]

When VO_2 is placed under pressure, two other phases emerge. M2 is similar to M1 in that the Vanadium ions pair up and dimerize, but the V^{+4} pairs do not twist off-axis, and only every other row dimerizes. There is also a triclinic T phase.[**?**] However neither of these phases appear in our films, and are not relevant to this work.

Along with the change in lattice structure, there is a large shift in the electronic bands, changing it from a poor insulator to a dirty metal when heated. Unfortunately, the band structure in VO_2 is difficult to qualitatively calculate from first principles, leading to continued debate as to what is the primary transition mechanism. In the next section I will outline why this is the case.

2.1.2 Band Theory

As anyone who works in condensed matter knows, modeling crystalline materials is not a trivial task. A Hamiltonian that accounts for all the coulomb potentials between all the ions and all the electrons in the system becomes prohibitively complicated to compute. The most naive way of simplifying the problem is to use the Free-electron model. We assume that the ions in the background are smeared out to be a constant positive background, and the electrons behave as a gas. From the resulting electron density, one can calculated what the plasmon frequencies are, and what electromagnetic wavelengths are absorbed or reflected in metals. The Dirac-Smith equation is used calculate the conductivity in materials probed with THz:

$$\sigma_{DS} = \frac{ne^2\tau_{DS}}{m^*(1-i\omega\tau_{DS})}(1+\frac{c}{1-i\omega\tau_{DS}}) \tag{2.1}$$

where ω is the frequency of the light, n is the number of free electrons, m^* is the effective mass of the electrons, and τ_{DS} is the scattering time of the electrons due to impurities and grain boundaries. For smaller wavelengths, you don't have to consider grain boundaries, since the E&M field causes the electrons to change direction before they can scatter off a boundary that would change the conductivity of the material. [15]

This a useful, but highly simplistic model, and doesn't explain why some materials are insulators and some are metals/semiconductors. Soon after the discovery of quantum mechanics, there were several people proposing that solids have energy bands that electrons can be in. [**?**]

This periodicity of the lattice results in the electrons having forbidden energy regions, or gaps in which the electrons are forbidden. We can then fill the lattice with lots of electrons (assuming that there is no interaction between electrons) and Pauli's exclusion principle means that the electrons must fill these energy bands. If the Fermi level lies within a band then, the material is metallic, since it is easy for the electrons with the highest energy to be excited enough to be mobile. If the Fermi level lies within a band gap, however, then the there is a much higher energy cost to excite the electrons to be mobile, and the material is considered to be an insulator. Semiconductors have the fermi level within a gap, but the gap is small enough that electrical conductivity is not as difficult to achieve as for an insulator.

Because we are assuming the electrons are not interacting, this is still a simplistic model, but it is still an effective one for many materials. However, it was soon discovered that the transition metals, with partially filled d orbitals, were behaving like insulators, even though traditional band theory would predict that they are metallic.[2] Pierls was the first to suggest that electron-electron correlations play an important role in these insulators. It was Mott, however, that came up with the model for the Mott insulator. He described a 1D lattice where each lattice sits on a lattice site, and if you ignore coulomb forces, a band fills when there are two electrons at each site (one spin up the other spin down). But if the electrons start to interact strongly, then any second electron at a lattice site will feel a repulsion from the first electrons, and the energy cost of placing an electron there will be higher. This leads to a splitting of the band, and the lower energy band is now full when each lattice site has an electron.

Now some of these Mott insulators can transition into metals. Figure 2.1.2 shows two paths for a metal-insulator transition can happen based on the Hubbard model, where electron behavior is dependent on U, the energy cost of placing an electron at a lattice site, and t, the transfer engergy it takes to transfer an electron from one site to another. (See—-)One path to MIT is filling controlled, where fewer electrons inhabit the valence band, and the importance of U goes down. In band-controlled MIT, the filling of the bands staying the same, but the band structure changes.

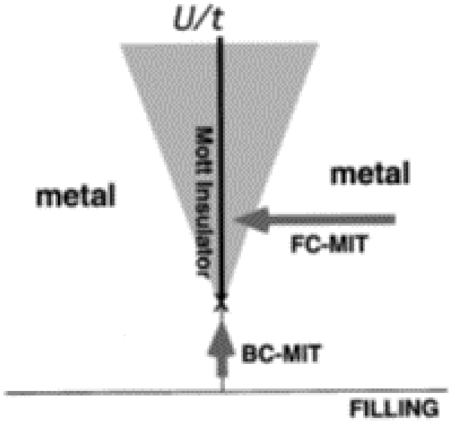

FIG. 2.2: Here is a graph based on the Hubbard model, showing two avenues that a material could go through a insulator-metal transition. The band-controlled model changes the relationship between U and t, creating localization do to the energy cost of moving electrons. The filling controlled model changes the number of electrons in a band, which makes U play a larger role in increasing the energy cost of moving electrons within the lattice[2]

2.1.3 Insulator-Metal transition in Vo_2

VO_2 is a one of the transition metals, and like the other transition metals, is a highly correlated material. Theorists are still working to quantitatively model the transition, but have met with difficulty coming up with a model from first principles that both works for the low temperature insulating monoclinic phase and the high temperature metallic phase. Goodenough in the 60s made a calculation of the band structure in both insulating and metallic phase, based on spectroscopic data.[1] There are two bands that fall on the Fermi level. One is the $d_{||}$ orbitals from the VO_2 orbitals, the other is the π^*, which comes from the hybridization with the oxygen ions.

What makes VO_2 more complicated than other materials that go through an insulator-metal transition, is that there are two mechanisms at play. At low temperatures the $d_{||}$ band splits, with one below the fermi level and one above. At higher temperatures the bands collapse, making VO_2 metallic. There is also a shift in the π^* band to below the Fermi level. However, this band collapse is accompanied by the lattice going to the higher symmetry tetragonal phase. The V^{+4} ions are no longer diamerized, which changes the shielding of the valence electrons, which would affect the electron-correlation, as well as shifting the overall energy of the bands in a Pierls type transition (See——). The question, which researchers have been struggling with since VO_2 was discovered, is which mechanism is the primary driving mechanism of the insulator-metal transition. There are several different ways researchers initiate the transition, with the hope that the different resulting behavior will tease apart the two mechanisms. There is heating of course, as well as voltage application, doping, pressure, and optically pumping the material. One promising avenue of study, which our experiments are based on, is looking at time resolved optically pumped measurements.

2.1.4 Optical properties of VO_2

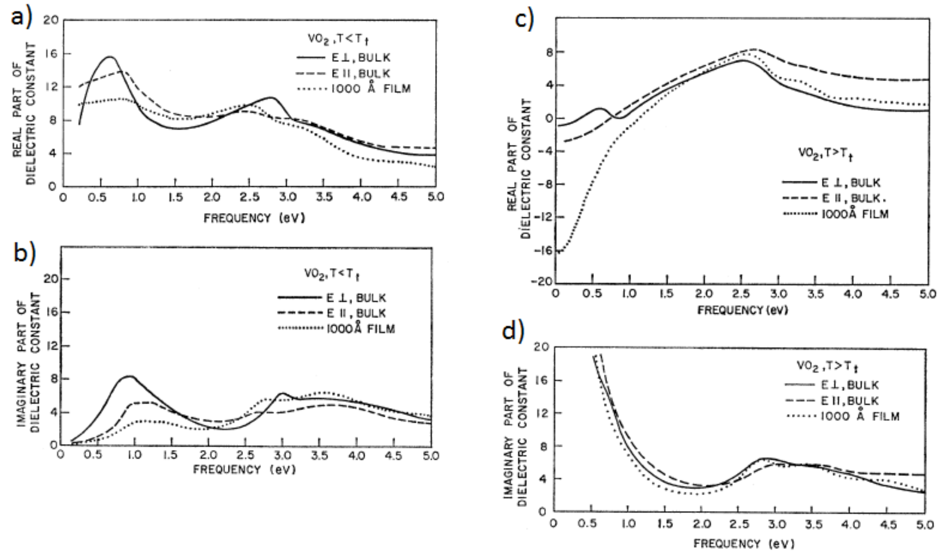

FIG. 2.3: Measured complex dielectric constants for VO_2, both in bulk and for a 1000 film on Al_2O_3. a) is the real part of ϵ , and b) is the imaginary part at room temperature, and c) and d) show the same for the material heated up to 355 K. From Ref. [3].

Ultrafast studies of VO_2

With the development of laser pulses that were on the femtosecond scale, there was soon an interest in looking at the time dynamics of the VO_2 metal-insulator transition. The hope was to separate the response of the lattice from the faster electronic response. With the advent of ultrafast lasers, there arose a new avenue of study of the insulator-metal transition in VO_2.[16] Sufficiently short light pulses can photoexcite the electrons in a material before the lattice has time to respond (response time of typically?). By picking a photon energy that is sufficient to photoexicite the electrons above the band gap, it is possible to quickly induce the transition.

Because the debate about the primary mechanism of the VO_2 phase transition is between a Peierls type transition and a Mott type transition, one of the ways that ultrafast studies can contribute to the debate is to look at the rate of change in transition. Elections can respond on a sub-femtosecond scale, so electronic responses in the film will appear to happen within femtoseconds of the pump pulse hitting the sample, while the lattice will take picoseconds to respond. The time it takes for the excited electrons to transfer energy to the lattice will take on the order of tens of picoseconds.

The first pump-probe studies were unable to measure the limit of the switching time [17, 16] due to the limit in pulse durations available. Only once lasers were able to get down to the femtosecond regime could experimentalists realize how fast the insulator-metal transition could happen. Cavalleri found by varying the duration of the pump pulse that the transition has a bottleneck of 80 fs.[18] 80 fs is half a period of the 5-6 THz Ag modes that are believed to play a prominent role in the phase transition, since they map the M-VO_2 lattice structure to the tetragonal R-VO_2 lattice.

Hilton showed in PRL [19] that the threshold power changes when the sample is heated closer to the transition temperature, with less energy needed to induce the transition due to the softening of the lattice. Cocker et al.[20] expand upon this further by mapping out the threshold fluence for the VO_2 transition at a range of temperatures from 17-350 K. They find four different distinct behaviors in the dynamics of the insulator-metal transition. I discuss this in further detail in Chapter 5, as my experiment closely followed their process.

2.2 Known microstructures effects of the Films

The difficulty and gift of working with thin films is the variability in bulk properties that arises from the strain and grain boundaries. Bulk VO_2 has a very well defined transition temperature at 340 K, with a small hysteresis, although the insulator-metal transition is not repeatable due to the strain on the lattice cracking and deforming the material as it goes past T_c. Small nanocrystals of VO_2 will also exhibit transition temperatures close to bulk, repeatably since the smaller crystals has more surface area to accommodate for the lattice transformation. Studies have shown you can shift the T_c of these VO_2 nano crystals by applying pressure along the c_R axis, as well as putting the material in the M2 and T phases.

This shifting of T_c also happens with highly strained thin films. Compressive strain along c_R reduces T_c, while expansive strain will nudge the transition close to bulk T_c.[21]

CHAPTER 3

Characterization of heat induced MIT

3.1 Description of samples

All the samples I have used for these experiments were grown at University of Virginia. They were grown on substrates by Reactive Biased Sputter deposition. We received films grown on SiO_2, Al_2O_3, and one on TiO_2. Because of the similarity of the insulator-metal transition for the VO_2 films on Al_2O_3, most of the work here focuses on the difference between the films on TiO_2 and Al_2O_3.

We were given a series of film thicknesses grown on Al_2O_3 ranging from 50 nm to 100 nm. The film grown on SiO_2 is 80 nm and the film grown on TiO_2 is 110 nm.

3.2 Continuous Wave Reflection and Transmission measurements

The primary way I have characterized the insulator-metal transition in our VO_2 thin film samples is by looking at the reflectivity. I have also looked at the transition by measuring the conductivity with a four-point probe, and measuring the Raman peaks with a Raman spectrometer.

3.3 X-Ray Diffraction

Another technique we used to characterize the samples was X-Ray diffraction (XRD). XRD is an essential technique to determine the crystallinity, thickness, and strain in our films. In a crystal, periodicity in the lattice will create maxima when x-rays reflecting off the planes of a lattice have a path length that leads to constructive interference between layers. Depending on the symmetry of the crystal, each material will have an individual XRD fingerprint, which allows us to identify what is contained in the sample. So XRD is an important tool for determining if our films are really VO_2 and not some other Vanadium oxide. It also give us a wealth of other information: such as the orientation and thickness of the films, whether the films are mono-crystalline or polycrystalline, the size of the grains, and the strain due to mismatch with the substrate. These characteristics affect the properties of the insulator-metal transition, and are considered in our analysis for the experiments in this work.

Figure 3.1 shows the basic principle behind XRD. Since x-rays are on the same length scale as lattice spacings in crystals, we can use the interference between layers to calculate the distance between planes with Bragg's Law. If one is using an X-ray source with a fixed wavelength, one must consider the geometry of your x-ray source and the detector. Each

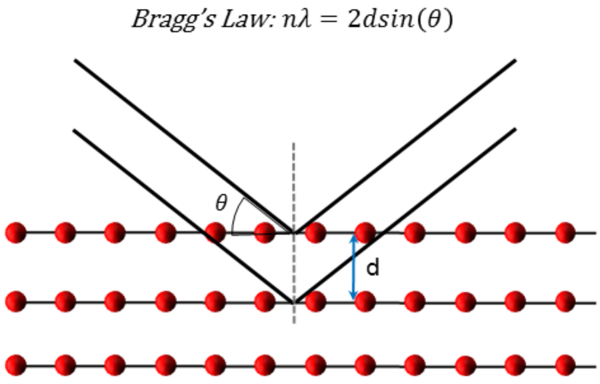

FIG. 3.1: X-ray diffraction uses the interference between layers in a crystalline material. The x-rays will constructively interfere when Bragg's Law (as shown above) is satisfied. By scanning over θ we can find for what angles there is a diffraction point, and from there calculate d.

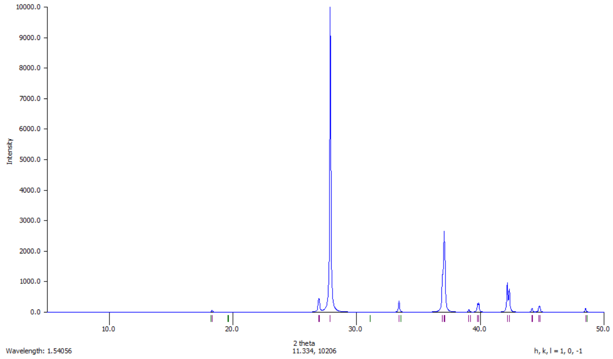

FIG. 3.2: This is a calculated powder XRD pattern of M1-VO_2. The peaks we see in our $\theta - 2\theta$ measurements are consistent with the peaks seen here.[4]

set of planes are going to constructively interfere at a specific angle, so in order to get a complete picture of the crystal you need to measure over all the incident angles ($\theta - 2\theta$). If your sample is powdered, your XRD measurement will contain all possible XRD peaks since you have many different nanocrystals in different orientations. But for epitaxial thin films, the peaks that you can see over a 2θ scan depends on the orientation of the film. This requires us to rotate the film to different orientations to access different peaks not accessible when the film lies flat. Figure 3.3 shows how the stage can rotate. Tilting the stage about χ lets us access crystalline planes of different orientations. Rotating about ϕ tells us if there is more than one crystalline orientation within the films; if there are several peaks when we rotate about ϕ then there was more than one preferred orientation when the film was grown on the substrate.

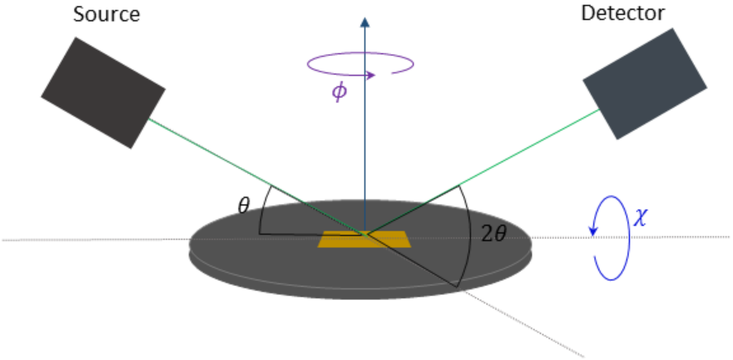

FIG. 3.3: In order to access different family of planes within a thin film sample, it is necessary to rotate the stage. $\theta - 2\theta$ scans are when the source and detector move to change the incident angle of the x-ray beam. ϕ rotates the stage about the normal of the sample surface. χ tilts the stage, rotating the sample's normal with respect to the incident beam.

A cathode ray tube makes the source of the x-rays with a wavelength corresponding to Cu K-α, which has a wavelength of 1.54 . We used a commercial system Empyrean from Paralytically, which is particularity well suited to measure XRD of thin films, due to it's rotating stage.

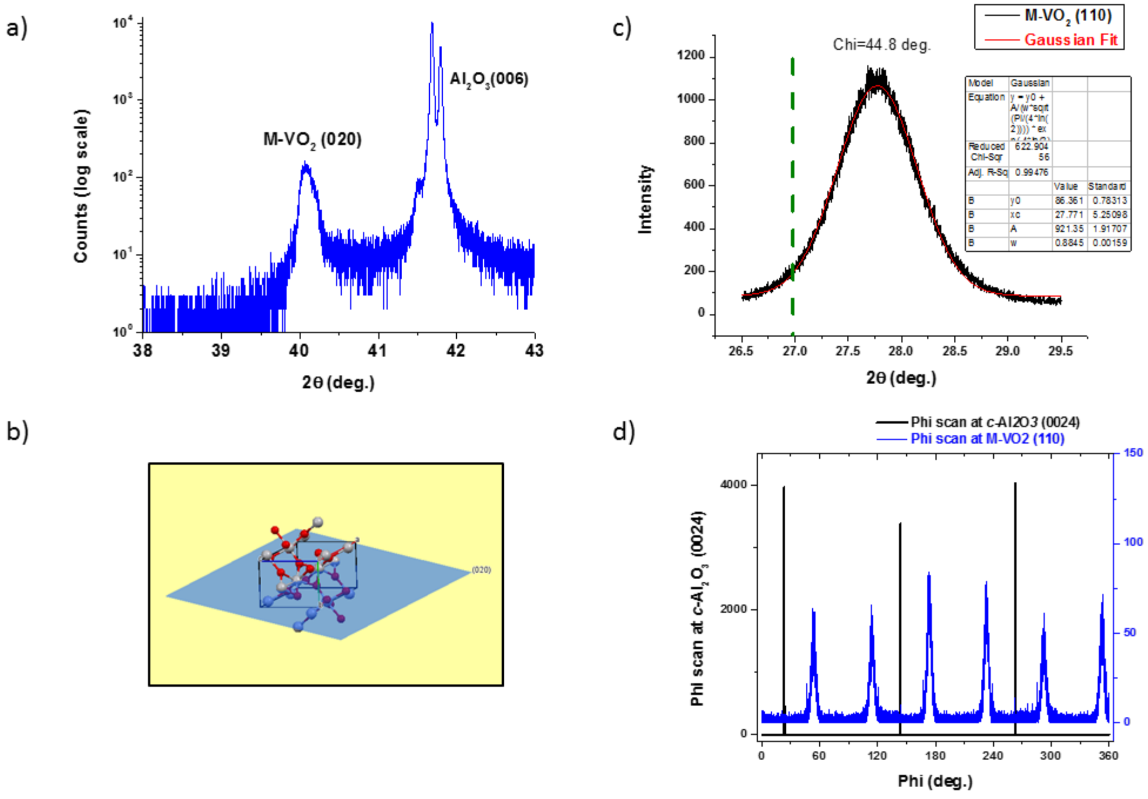

FIG. 3.4: Here is the XRD data from VO_2 on Al_2O_3. a) shows the $\theta - 2\theta$ curve, which shows the strong substrate signal and the weaker VO_2 peak. Because the x-ray source has both Cu K-α1 and K-α2, the narrower substrate peak narrow enough to resolve both wavelengths. b)is a depiction of the (020) plane in M-VO_2. c) is an asymmetric $\theta - 2\theta$ scan at χ=44.8° of the M-VO_2 plane (011). d) shows the ϕ-scan at $\chi = 44.8$, showing 3-fold symmetry.

Figure 3.4 shows the XRD measurements for the 80 nm VO_2 film on Al_2O_3 (thickness measured with x-ray reflection measurements). We identify the substrate peak of as being the strong signal on the right in figure 3.4 a), and a single peak from the film. This peak corresponds to the (020) M-VO_2 plane. As this is the only peak from the film for the symmetric scan, we can infer there is only one crystal orientation out of plane.

From the asymmetric scan in figure 3.4 c) we identified the M-VO_2 (110) peak at $\chi = 44.8°$. The ϕ scan shows six peaks from the film, which corresponds to a 3-fold symmetry in the film. This makes sense when we consider how M-VO_2 would map onto the substrate. The substrate is c-cut Al_2O_3 which is trigonal and looks like an array of hexagons from above. Since $\gamma = 123^{circ}$ [14], it would naturally deposit on the substrate in 3 possible orientations, with (020) pointing up. This film is crystalline, and from the shift of the peak relative to the bulk peak position, it has an in-plane strain of -0.53% and an out of plane strain of -2.81%.

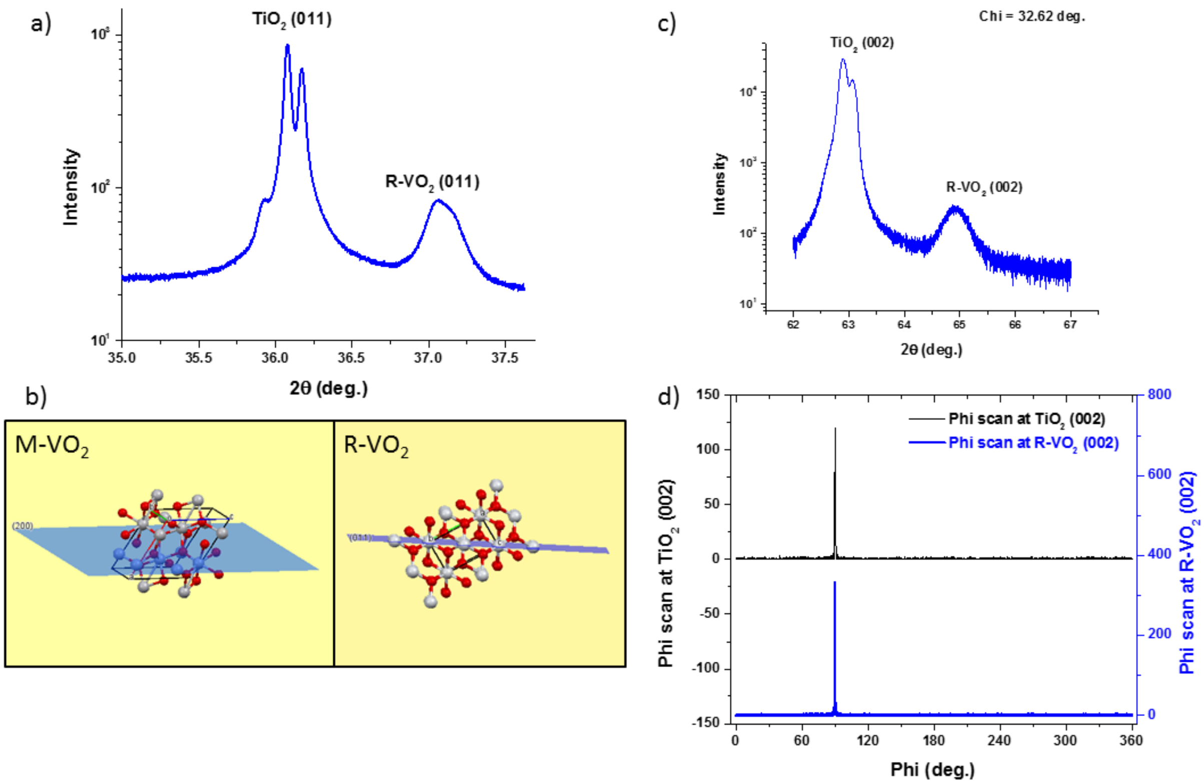

FIG. 3.5: Here is the XRD data from VO_2 on Al_2O_3. a) shows the $\theta - 2\theta$ curve, which shows the strong substrate signal and the weaker VO_2 peak.

Figure 3.5 a) shows the symmetric $\theta - 2\theta$ scan for the 100 nm VO_2 film on TiO_2. The TiO_2 (011) substrate is tetragonal, like R-VO_2 phase, so it's a natural material to grow VO_2 films on. The symmetric $\theta - 2\theta$ scan gives us a film peak at 37.1^deg. This could correspond to either M-VO_2 (200) or R-VO_2 (011). As shown in figure 3.5 b), those planes represent the two different phases in the same orientation. The ϕ scan shows a single peak, which tells us there is a single crystalline orientation and the film is truly mono-crystalline. The strain out of plane is 0.14% and in plane is 0.53%.

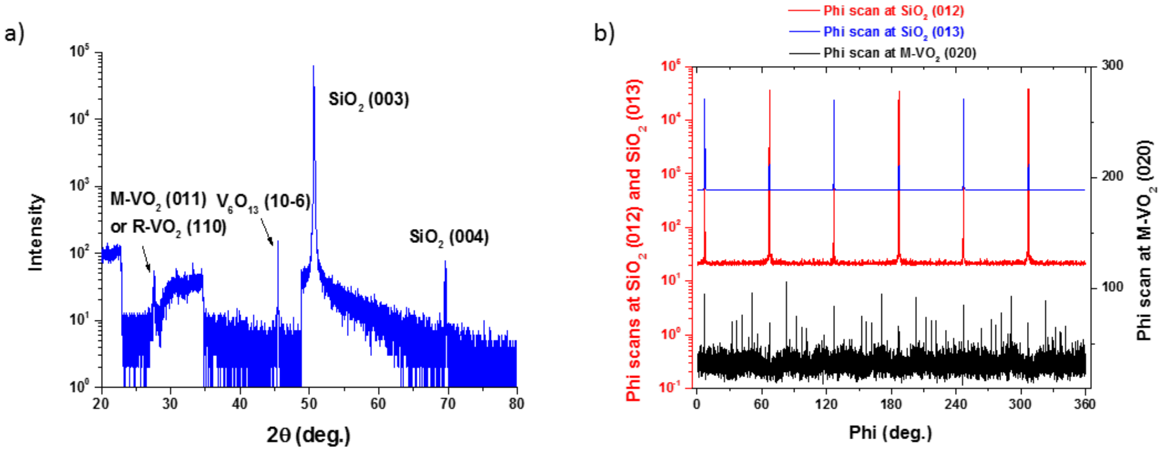

FIG. 3.6: Here is the XRD data from VO$_2$ on Al$_2$O$_3$. a) shows the $\theta - 2\theta$ curve, which shows the strong substrate signal and the weaker VO$_2$ peak.

The XRD scans for VO$_2$ on SiO$_2$ shown in figure 3.6 show a single M-VO$_2$ peak at $2\theta = 27.61°$. There is another peak at $\sim 45°$, but that is associated with another oxide, which means this film is not as pure as the others. But it does have a single orientation out of plane. The figure 3.6 b) shows a ϕ scan which is different from the ones for the previous two samples. There are not clear peaks, meaning there is no preferred orientation when the film was grown on the substrate and is polycrystalline. There is an out of plane strain of 0.92%.

3.3.1 Grain size

The width of the peak in XRD measurements can also tell us the average grain size. The relationship between the peak width is defined by the Scherrer equation[22]:

$$B_{crystal} = \frac{k\lambda}{L cos\theta} \tag{3.1}$$

where $B_{crystal}$ is the width of the XRD peak, k is a constant based on the shape of the grains in the film, L is the average grain size and θ is the Bragg angle. For the films grown on Al_2O_3, TiO_2, and SiO_2 we find an average grain size of 65 nm, 12 nm , and 20 nm respectively.

3.4 Continuous Wave Measurements

When a material's conductivity changes, the optical properties will change as well, since light is an electromagnetic wave. The susceptibility of a film depends on the band structure.

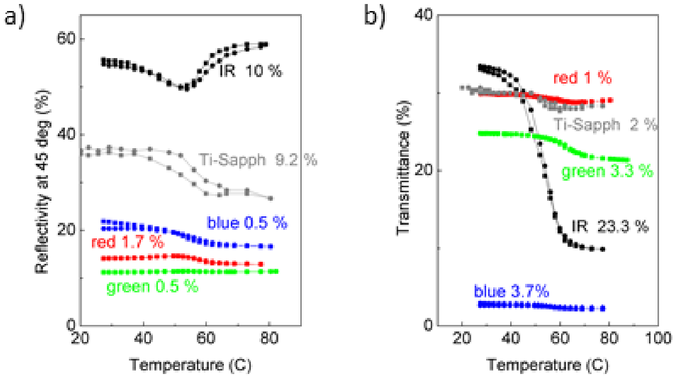

FIG. 3.7: Here are measurements taken by Ceasar 'Blank' and Irina Novikova looking at the reflection (a)) and transmission (b)) for VO_2 on –. As we move from visible light into the infrared regime, the response becomes more dramatic for both transmission and reflection.

Figure 3.4 shows the IMT with measured with several different wavelengths, in both absolute transmission and reflection. The transition is not that impressive until we get to 800 nm, where the absorption increases through the transition. In the infrared we see it behaving as we would expect a metal to, where the reflection increases and the transmission decreases. In figure 3.4 we can see that the visibility of the transmission has a dependence on λ. The reflection and transmission do not change much with the insulator-metal transition in the visible light regime. Once we get to 800 nm we see a large amount of absorption, as both transmission and reflection drop as the film goes through the transition. At 1520 nm we see the most profound transition, with a 10% increase in reflection and a 23% drop in transmission. This is why VO_2 has been proposed as a candidate for a coating for smart windows. Because the reduction of infrared transmission is so much more than for visible light, you can reduce IR radiation from the sun with out darkening too much.

Our cw measurements were primarily with 800 nm, as this is the wavelength of our ultrafast pulses, and the signal is reasonably large when looking at the reflection. The experimental set up, as shown in figure 3.8, is not terribly complicated. The beam is reflected off the surface of the VO_2 sample, and both transmission and reflection can be measured as the film is heated through the transition. A half-wave plate allowed us to look for anisotropy in the transition by changing the polarization of the incident beam. Films were mounted on a Peltier that allowed us to control the temperature of the films. The temperature was monitored with a 10 kω resistor and controlled with a TEC controller from Thorlabs.

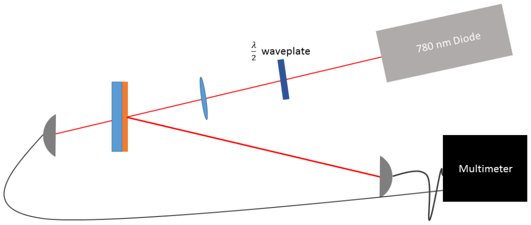

FIG. 3.8: The experimental set up of our continuous wave measurements. Beam was focused on sample, and the polarization of the incident beam was controlled with a half-wave plate. Films were mounted on a peltier heater allowing us to control the temperature. We looked at both transmission and reflection measurements.

Figure **??** shows the change in reflection as we heat VO_2 through the insulator metal transition for the 100 nm samples on Al_2O_3, TiO_2, and the 80 nm sample on SiO_2. The reflection is normalized with respect to the intensity of the reflection at room temperature. It is clear that the different films have noticeable differences in their transitions. The transition temperature (T_c) of VO_2 on TiO_2 at 310 K is much lower than then the T_c of VO_2 on Al_2O_3 or SiO_2. The T_c for VO_2 on Al_2O_3 is much closer to bulk at 340 K, and for VO_2 on SiO_2 T_c=326 K. The width of the transitions are quite different for these samples as well, 26 K, 9 K, and 15 K respectively.

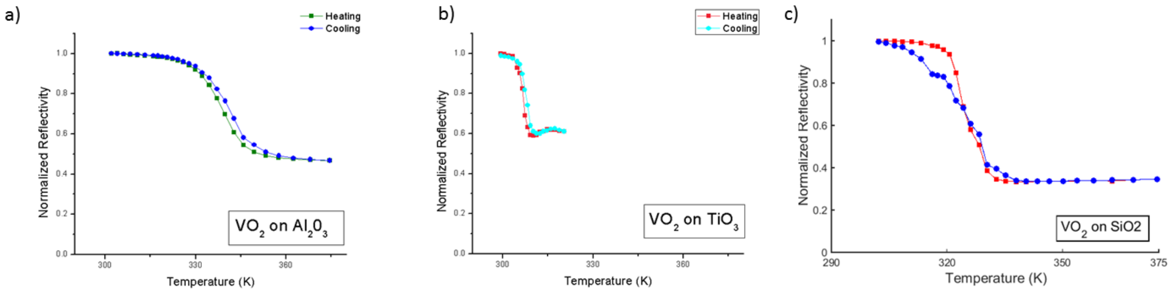

FIG. 3.9: Here are continuous wave measurements of the reflection off of VO_2 on a) Al_2O_3, b) TiO_2, and c) SiO_2, taken with a 780 nm diode laser. The reflection drops as the films are heated through the transition, and we see all the films show the characteristic hysteresis of the transition. Each film has a very different transition temperature T_c and transition width, which can be explained by the different microstructures we found in each film.

These differences are not surprising when we consider the differences we see in the microstructure of the films from XRD. The film on TiO_2 is monocrystalline, and therefore is likely to have fewer defects from lattice mismatch; this is reflected in the narrower transition. It also has the lowest transition temperature, that is due to the fact that the substrate is has a tetragonal lattice structure, like the R-VO_2 phase. This is reflected in the fact that the phi-scan has a tetragonal symmetry like R-VO_2, meaning that the film is clamped in the R-VO_2 phase. From the Raman measurements, as described in section 3.5 below, we see modes associated with M-VO_2, so it's probable that there is a mix of the two phases at room temperature. This will lead to a higher strain in the film when it's in the M-VO_2 phase, bringing down the energy needed to drive the transition. Other works have shown you can control the T$_c$ depending on how much of a mismatch you have between VO_2 and the substrate.[23, 10, 21] While our measurements do not show much strain in the peak, the lower T$_c$ is likely the result of clamping.

On the other hand, the film on Al_2O_3 has a almost bulk like transition temperature, and the width of the transition is much broader. The average grain size is much higher and there is a connection between the grain size and the T$_c$ of the individual grains. [24, 25, 26] We can infer that we do have a distribution of grain sizes from the bi-chromatic measurements taken by L. Wang et al. [27] Different wavelegnths have a different T$_c$ for the same sample. Different wavelengths are going to be sensitive to different length scales, so a distribution of grain sizes would lead to this broadening of T$_c$.

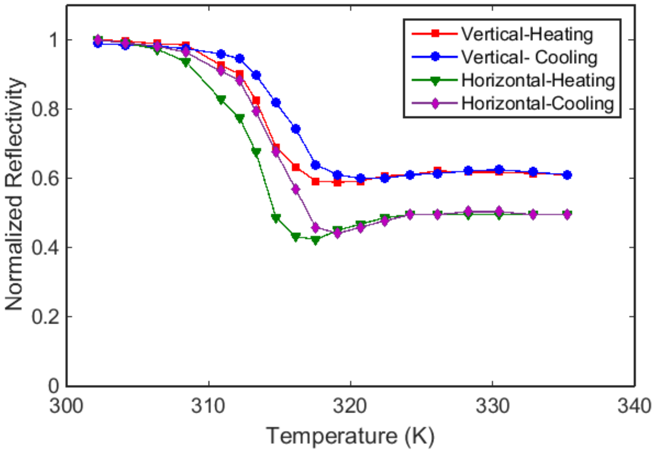

FIG. 3.10: Here is the normalized reflection off of VO_2 on TiO_2 at 780 nm. The change in reflectivity is different depending on the orientation of the film, due to the mono-crystalline nature of the film and the anisotropic nature of VO_2.

One way in which the film of VO_2 on TiO_2 is unique from the other samples is that the transition is anisotropic. Bulk VO_2 is anisotropic, but most of our films have multiple orientations with in the plane, and so there is no preferred direction for reflectivity. However, VO_2 on TiO_2 is a monocrystalline film, and shows a difference in both conductivity and optical properties depending on the orientation of the film. Figure 3.10 shows the normalized reflectivity along the two different orientations. There is a noticeable difference in the drop in reflection along the two different axies. This is consistent with previous measurements on comparable films.[10]

3.4.1 Modeling Reflection and transmission

When dealing with thin films, the overall transmission and reflection are going to depend on the thickness of the films, as well as the optical properties of the layers. In order to model the reflection and transmission, I calculated a 4 transfer matrix using the method outlined in Shubert's paper.[28] While this is normally a straight forward calculation with an isotropic material, it becomes a much more involved calculation when you include anisotropic layers with random orientations.

In order to calculate a transfer matrix for a series of optical elements, you multiply the transfer matrix for each individual element in reverse order that the beam travels through it. For series of thin films the transfer matrix will look like:

$$T = L_a \prod_{i=1}^{N} T_{ip}(-d_i) L_{out} \tag{3.2}$$

where L_a is the matrix for the interface between the incident medium and the first layer, L_{out} is the matrix for the interface into the exit medium, T_{ip} is the partial transfer matrix for the i'th layer, and d_i is the thickness of the i'th layer.

I wrote up a program in MATLAB which calculates the reflection, transmission, and absorption using the general calculation for the partial transfer matrices of a randomly oriented anisotropic crystal. Using index of refraction from ellipsometry and from previous studies [3] I used these calculations to check that our measurements were consistent with VO_2.

3.5 Raman Spectroscopy

3.5.1 Raman Scattering

Raman scattering is an inelastic process where light reflected off a sample will be partially absorbed by a vibrational mode in the sample, and will there for have a frequency shift due to the lowering of energy.

Vanadium dioxide (VO_2) undergoes a well-known structural phase transition, changing from a monoclinic lattice structure to a tetragonal lattice structure accompanied by up to six orders of magnitude increase in the conductivity and consequent changes in the optical properties.[6, 14, 29] The fact that this metal-insulator-transition (MIT) in VO_2 occurs just above room temperature (340 K for bulk) makes it an exciting prospect for many new technologies. For example, it offers a low loss alternative to noble metals for plasmonic applications,[30] development of smart window coatings,[31, 32] novel electronic devices,[33, 34] etc. Also, the MIT can be optically induced in a sub-ps timescale,[35, 36, 37, 38] making VO_2 an attractive material for ultrafast optical switches and sensors. In this paper, we experimentally investigate the effects of different microstructure in VO_2 films by comparing their optical properties for films grown on c-Al_2O_3 (sapphire), crystalline SiO_2 (quartz), and TiO_2 (rutile) substrates. We have monitored the thermally induced changes in the VO_2 structure using two complementary optical techniques, namely Raman spectroscopy and optical reflectivity of a weak 780 nm laser. The two phases of VO_2 have distinct Raman signatures: The insulating monoclinic phase (at low temperature) displays several sharp Raman peaks, and at temperatures above the transition temperature the Raman spectrum of the metallic rutile phase is characterized by a broadband emission.[39, 40, 41] While we observed this typical behavior in all samples, this transition occurred at a lower temperature for the samples grown on rutile and quartz, compared to those grown on sapphire. Complementary measurements of the optical reflectivity showed a similar trend. A comparison of the crystalline microstructure of the samples shows correlation between the measured temperature at the onset of the phase transition and the average grain size of the different films investigated, consistent with some theoretical predictions.[24, 25, 26] We also experimentally found a wavelength for the excitation laser leading to optimal VO_2 Raman spectra, and found that the near-IR (785 nm) laser yielded the best resolution.

3.5.2 Raman spectroscopy experimental set up

The VO_2 thin films, used in our studies, were prepared using Reactive Biased Target Ion Beam Deposition (RBTIBD), described at length elsewhere.[38] The thickness of the VO_2 films grown on quartz and sapphire substrate was 80 nm, whereas the sample grown on rutile substrate had a thickness of 110 nm. The microstructure of the VO_2 thin films was characterized by X-ray diffraction (XRD) using a Rigaku diffractometer with Cu Kα radiation. The detailed characterization procedure of the samples is presented in Ref. [30]. Our analysis demonstrated that the VO_2 film grown on quartz substrate was textured and M-VO_2 (011) is the main out-of-plane reflection. However, it had no preferred in-plane orientation, indicating that the sample is polycrystalline. The film grown on sapphire had epitaxial structure, with (020) out of plane orientation. A ϕ scan revealed a 6-fold symmetry in the plane of the film consistent with previous reports stating that VO_2 exhibits twin-domain epitaxial growth on c-plane sapphire with a triple-domain (020)epitaxial structure with six-fold rotational symmetry in the basal plane.4 The film grown on rutile exhibits a crystalline structure with a (011) orientation, matching the substrate. Prior studies on these films indicate that VO_2 acquires tetragrutile VO_2. The average grain size estimated applying the Scherrer equation[22] to the half-width at half maximum (HWHM) main XRD peaks was 20 nm for the sample grown on quartz while the VO_2 film grown on c-sapphire exhibited an average grain size of 65 nm. Since the film grown on rutile is strained, which can also affect the peakâĂŹs HWHM, we could only estimate a lower limit average grain size for this sample of 12 nm.

For the optical characterizations, the samples were mounted on a thermoelectric cooler (TEC) element, connected to a precision temperature controller able to vary temperature from 20 °C to 90 °C. A miniature 10kΩ thermistor, pressed down with thermal conducting paste onto the surface of the sample, monitored the film temperature throughout the measurements. To monitor the changes in the optical properties of the films as they underwent thermally induced MIT, we used two complimentary optical detection methods. In the first case, we measured changes in reflection of a 780 nm diode laser due to changes in the optical conductivity of the VO_2 samples through the MIT. Second, we observed the modifications of the VO_2 samples microstructure through the MIT using Raman spectrometry. The Raman spectra, shown below, were obtained with a Kaiser Raman Rxn1 microprobe using a 50× magnification objective that provided spatial resolution of 11 μm, and a depth of focus of 2 μm. This instrument is configured to operate at three different wavelengths for optical excitation: 532 nm (25 mW), 632.8 nm (3.5 mW), and 785 nm (7.58 mW), allowing us to compare the VO_2 Raman signal at these different optical wavelengths.

3.5.3 Results and discussion

Examples of experimental Raman spectra measured at the low-temperature phase (monoclinic) of the VO_2 sample grown on quartz are shown in Fig. 3.5.3. Group theory predicts a total of eighteen Raman active phonon modes in the low-temperature (insulating) regime: nine Ag modes and nine Bg phonon modes that have been identified in previous works.[39, 40, 41]

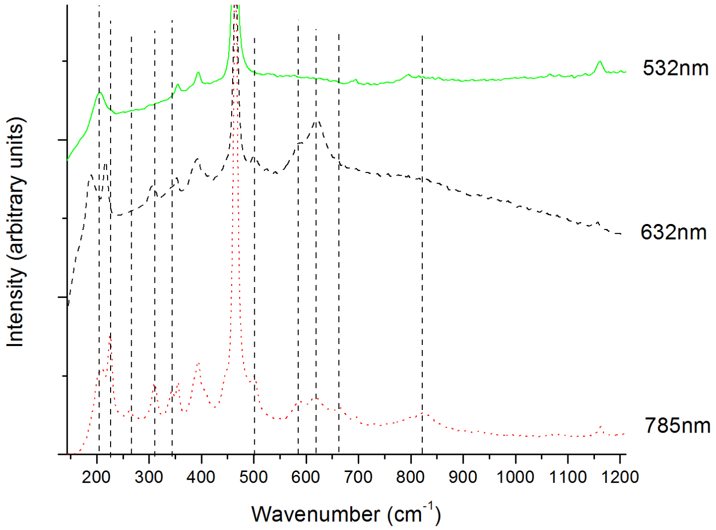

FIG. 3.11: Raman spectra for VO_2 thin films deposited on quartz substrates obtained using different excitation lasers.

In our samples, we have observed a majority of these identified modes (summarized in Table 3.5.3). It is important to note that we found none of the peaks associated with other forms of vanadium oxides, in particular, V_2O_5 that has a similar Raman signature. This fact offers good evidence of the high purity of the VO_2 composition in our samples. There are twelve clear VO_2 peaks (ten peaks detectable in the VO_2 on the sapphire sample are identified by dashed vertical lines in Fig. 3.5.3): 198 cm^{-1}, 225 cm^{-1}, 265 cm^{-1}, 309 cm^{-1}, 342 cm^{-1}, 439 cm^{-1}, 481 cm^{-1}, 501 cm^{-1}, 595 cm^{-1}, 617 cm^{-1}, 660 cm^{-1}, and 810 cm^{-1}. However, on the film grown on sapphire, we have also observed several additional Raman peaks including one near 1075 cm^{-1}, which exhibit temperature dependence consistent with the MIT transition. Moreover, the Raman frequencies of these peaks do not match any of previously identified phonon modes in monoclinic VO_2, and they lie beyond the expected Raman band for this material. Those peaks will require further study.

Figure 3.5.3 also shows a strong dependence of the detectability of the VO_2 Raman resonances on the excitation light wavelength. Notably, the clearest spectrum with maximum number of resolved resonances was observed with near-IR excitation ($\lambda = 785\ nm$), while only about half of the peaks were detectable with a red He-Ne laser ($\lambda = 633\ nm$). For even shorter wavelength ($\lambda = 532\ nm$), the only visible Raman features were the substrate (quartz) Raman peaks. Such frequency dependence can be attributed to increased contribution of resonance fluorescence for higher-frequency radiation which increases the background and overwhelms any thin film contributions to the detected signal. Thus, our experiments suggest that it is advantageous to use a lower frequency optical wavelength to probe the Raman structure of VO_2 thin films. Since the Raman signature of the substrates was even stronger for the VO_2 films grown on sapphire and rutile, we were able to observe VO_2 Raman peaks only with the IR laser for these samples.

Schilbe13		Pan et al.14		Chen15		Present work	
Peaks	Modes	Peaks	Modes	Peaks	Modes	On quartz	On sapphire
149							
199	Ag	194	Ag			198	200
225	Ag	225	Ag	226	Ag	225	223
259	Bg	258	Bg	262	Ag	250?	No
265	Bg	265	Bg	264	Bg	262	266
313	Ag	308	Ag	311	Bg&Ag	309	308
339	Bg	339	Bg	339	Ag	342	339
392	Ag	392	Ag	390	Ag	Blocked	
395	Bg	395	Bg	395	Bg	Blocked	395
444	Bg	444	Bg	444	Bg	439?	443
453	Bg	453	Bg	454	Bg	Blocked	453
489	Bg	489	Bg	483	Bg	481	486?
503	Ag	503	Ag	500	Ag	501	497
595	Ag	585	Ag	591	Bg	595	âĂę
618	Ag	618	Ag	618	Ag	617	616
670	Bg	650	Bg	662	Bg	662	660
830	Bg	825	Bg	826	Bg	810	825

TABLE 3.1: Comparison of measured monoclinic VO_2 Raman resonances with previously reported results.

Figure 3.5.3 shows examples of Raman spectra taken at different temperatures above and below the insulator-metal transition for different VO_2 samples. The two possible

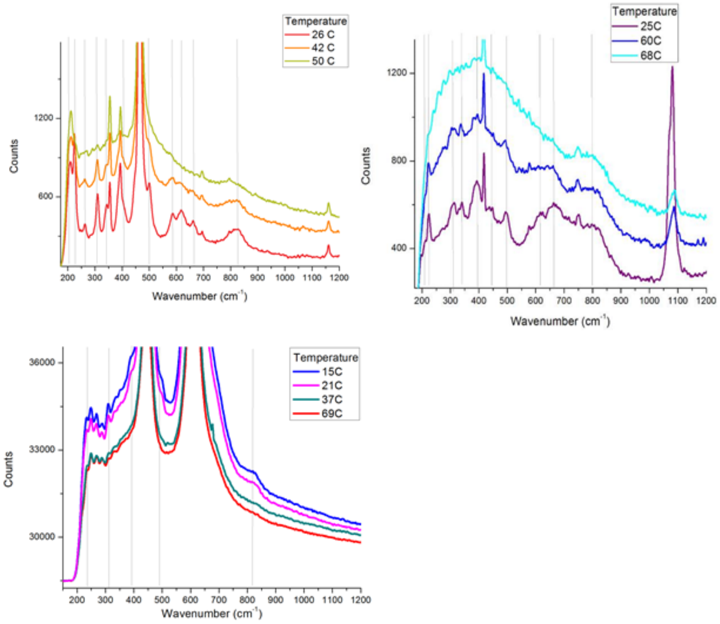

FIG. 3.12: Evolution of Raman spectra for VO_2 thin films deposited on (a) quartz, (b) sapphire, and (c) rutile substrates through the thermally induced MIT. Dashed vertical lines indicate expected positions of M-VO_2 Raman resonances. Unmarked peaks are substrate resonances. Two particularly strong rutile peaks are out of range in (c) in order to highlight the much weaker VO_2 peaks.

structures of VO_2 below and above the MIT temperature have distinctly different Raman signatures, clearly displayed in the experimental data. At low temperatures we observed the sharp spectral features associated with the monoclinic phase, while at higher temperatures we expect to see spectrally broad features associated with the tetragonal conducting phase, as indeed was the case. Thus, as the temperature of a sample increases, the amplitudes of the sharp monoclinic peaks decrease as the sample undergoes the transition. In our experiment, we have not observed any substantial difference between Raman frequencies of VO_2 monoclinic peaks for samples grown on different substrates, although depending on the substrate material, some of the expected resonances were obscured by the stronger substrate Raman peaks. However, as none of the substrate Raman features are temperature-dependent, it is possible to clearly identify any peaks that can be associated with a VO_2 film. It is interesting to note that in previous work[40] the phonon modes of different symmetry groups display different temperature behavior. However, in our experiment we observed no such difference. In particular, a 224 cm^{-1} peak (Ag mode) and 660 cm^{-1} (Bg mode) disappeared at the same rate for both samples when the films were heated.

On Figure 3.5.3, we display the thermal dependence of the optical properties of the VO_2 samples undergoing MIT: reflectivity measurements with a 780 nm cw laser (left column) and the amplitudes of some well-resolved Raman peaks, associated with the monoclinic VO_2 film (right column). We observed the characteristic reduction in optical reflectivity at the MIT critical temperature T_c.[3] For each of the three samples, we observe only a small difference between the transition temperatures for heating and cooling, manifesting a very narrow hysteresis (with exception of some low-temperature portion of the quartz sample). However, the temperatures at which this transition occurred were quite different depending on the substrate material. We observed the lowest transition temperature for VO_2 film grown on TiO_2, with a T_c=306 K. We see this for both sets of measurements,

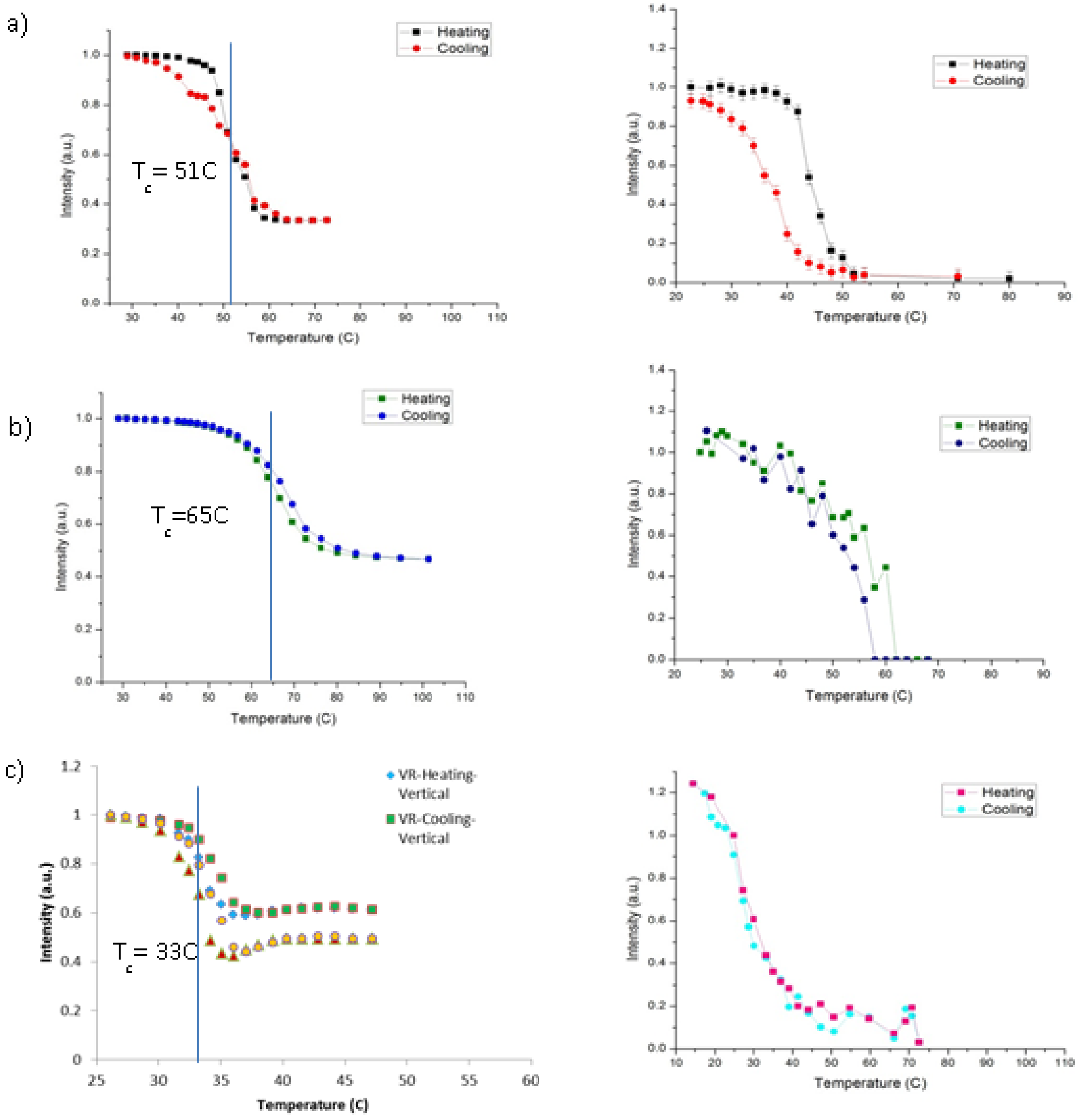

FIG. 3.13: Comparison of the MIT evolution for VO_2 thin films grown on different substrates. Left column: Reflectivity measurements with a 780 nm cw laser. Right column: Change in Raman peak intensity in each film. (a) VO_2 film on quartz, peak 224 cm^{-1}. (b) VO_2 film on sapphire, peak 224 cm^{-1}. (c) VO_2 film on rutile, peak 309 cm^{-1}. For the anisotropic rutile sample, the reflection for two orthogonal polarizations is shown. Some variation in transition temperature between the two detection methods may be due local heating due to focused pump beam in the Raman spectrometer. Vertical lines indicate the temperature for the phase transition temperature T_c .

namely the cw measurement and the rate of disappearance of the Raman peaks. For VO_2 on quartz and sapphire we see T_c=324 K and T_c=338 K, respectively. We note that MIT seemed to happen at lower temperatures in Raman measurements compared to the reflectivity measurements, most likely due to local heating of the sample by the Raman pump laser. For that reason, we use optical measurements for extracting the transition temperature.

The different behavior observed in the transition temperature for VO_2 thin films deposited under identical conditions but on different substrates can be attributed to differences in the microstructure of the films. Previous experiments have demonstrated that doping[32] and the size of the nanostructures[40, 42] can alter the average temperature of the phase transition, although the dominant effect in this case is broadening of the hysteresis loop. In our case, however, all three samples display a very narrow thermal hysteresis width, as seen in Fig.3.5.3.

We attribute the observed changes in transition temperature mainly to variation in the VO_2 film microstructure, mainly the average grain sizes. A proposed model, describing the properties of the MIT in thin films, considers the overall hysteresis curve as a combination of individual microscopic loops for individual VO_2 grains.[24, 25] In this model, it is postulated that in very thin films the grains are rigidly bound to the substrate and strain relaxation at the grain-substrate interface controls the temperature of the transition, and consequently the degree of strain relaxation upon nucleation determines the width of the thermal loop as well as the shift toward lower transition temperature as a function of grain size. Thus for an average grain size d, the structural transition occurs at a temperature

$$T_{film} = T_{bulk} - A/\sqrt{d} \tag{3.3}$$

where $T_{bulk} = 340\ K$ is transition temperature for the bulk VO_2, and A is a constant, determined by the material parameters of both the film and the substrate.[24]

We applied this model to our data using the average grain sizes estimated from the XRD data. We noted that indeed the smaller the grain size the lower is the transition temperature as the sample is heated. Table II shows the average values of the transition temperature from the optical reflection measurements, shown in Figure 3.5.3, average grain sizes and estimated value of constant A for all three substrates.

The narrowness of the observed hysteresis curves in the present case indicates absence of the elastic stress relaxations created during the initial transition. Thus, the reverse transition during cooling (from metal to insulator) occurs roughly at the same temperature, described by Eq.3.3, resulting in a narrow hysteresis loop shifted to lower temperature. We note that previous experiments, in which the size of the grains was varied by timed etching[24] or annealing[26] of the VO_2 film, also reported similar trend in transition temperature shift as a function of the grain size; however, in both experiments such shift was also accompanied by the broadening of the hysteresis resonance in stark contrast with our observations.

3.5.4 Conclusion

In conclusion, we observed that the Raman peaks associated with the monoclinic VO_2 insulating phase disappear at different temperatures upon annealing thin films of VO_2 deposited on different substrates. Since we observed a noticeable substrate effect on the films microstructure, we speculate that this change in the individual microstructure of each sample is responsible for the shifts in the MIT temperature. This difference in transition temperature was confirmed using optical reflection measurements. Specifically, we attribute this variation in transition temperature to the difference in average grain sizes in VO_2 films, thus opening an exciting avenue for tailoring the transition temperature for applications. An important advantage of the proposed model that we applied to our samples, compared to some previous proposals, is that the shift in transition temperature does not result in broadening of the MIT hysteresis, in agreement with our observations. We also compared the relative sensitivity of the VO_2 spectra using different wavelength pump lasers, and found that best spectral contrast was obtained with 785 nm laser excitation, due to reduced fluorescence background of the substrate material. This information will be useful for future investigations on thin VO_2 films, in which the low optical depth of the film results in a stronger Raman signature from the substrate.

CHAPTER 4

Ultrafast Pump-probe Experimental Set Up

4.1 Lasers

Lasers produce light by having a gain material, and some way to pump energy into that gain (either by electric current or another pump laser), and a cavity in which the light can build up by making several round trips.

4.2 Ultrafast Laser system

In order to take high resolution time measurements of the insulator metal transition, we can't simply use a photodiode with a continuous wave probe, the electronics in a photodiode can not response on a femto-second scale. In order to create laser pulses that are shorter than a picosecond one cannot use electronics in order to control the length of the pulse. Electronics are not fast enough in order to make pulses on the order of femtoseconds, so other tricks are required. If you have an infinite number of E&M waves that are different frequencies that have the same phase, by adding them all together you can get a delta peak. No gain medium is going to have a gain in all frequencies, but even with a reasonably large bandwidth, one can add them together to get a series of narrow peaks.

The difficulty in setting up an ultrafast system, then, is to find a gain material that has a sufficiently large bandwidth, and to force all the different frequencies to sync up, or 'mode-lock'. Many ultra-fast systems use Ti:sapph crystals, as the gain is —-.

Our oscillator mode-locks by passive mode-locking. Passive mode-locking occurs when the cavity length is varied rapidly. This changes the modes that the cavity can support, and if enough modes get in phase, then the Ti:sapph will saturate, and need time to recover. Other modes that are not in phase will not be able to lase outside this window and will die out. Eventually all the modes will be sync up in the time window that Ti:sapph allows.

Another reason that the Ti:sapph is an ideal material for making femto-second pulses is that it will further compress the pulse as it travels through the material due to the Kerr effect?.

The commercial laser system we use contains an oscillator (Mantis from Coherent), and an amplifier (Legend Elite from Coherent). The details on them can be found in appendix **??**.

4.3 Characterizing Pulses

4.3.1 Pulse duration

The commercial specs for the Legend-Elite amplifier say that the pulses coming out of they system are 100 fs long. When everything is optimal, this is a pretty good estimate.

However, ultrafast laser systems are very susceptible to lab conditions, so it is important to be able to confirm this.

One check we can do on the pulse duration is looking at the spectrum of the beam. If the spectrum has a certain bandwidth, that sets a limit on the minimum pulse width, as described by

$$\Delta\nu\Delta t \geq K \tag{4.1}$$

where $\Delta\nu$ is the bandwidth, and Δt is the duration of the pulse. This is a manifestation of the Heisenberg uncertainty principle. The larger the bandwidth, the shorter the pulse can be. This makes sense when one considers that one can move from frequency space to the time domain through a Fourier transform. We can also calculate Δt from the distribution of wavelengths (as measured with our Ocean optics spectrometer) with the relationship

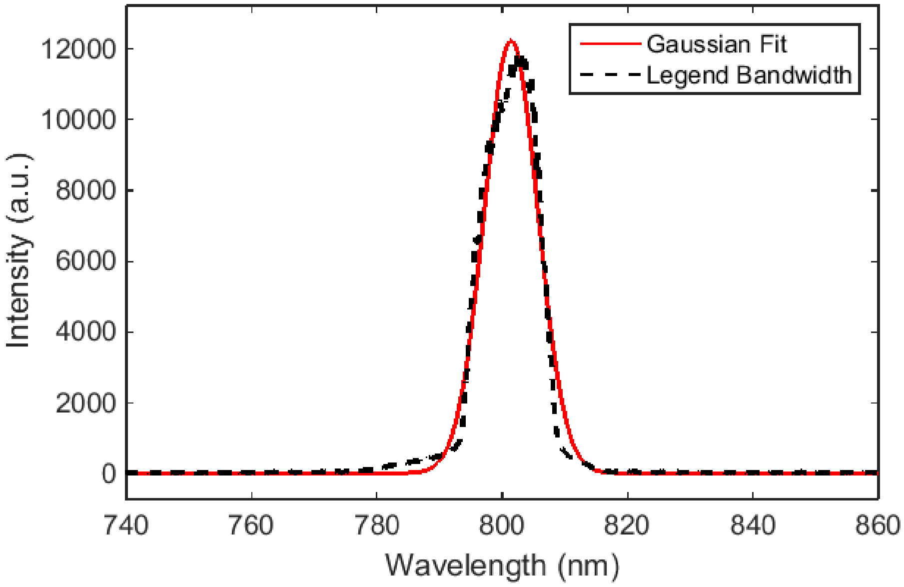

FIG. 4.1: This is the measured bandwidth of the ultrafast pulse coming out of the Legend amplifier (the pulses used for most of this work). By fitting with a Gaussian, we can get an estimate of the limit on the duration of the pulses coming out of the system.

$$\Delta t = K \times \frac{\lambda_\circ^2}{\Delta\lambda \times c} \tag{4.2}$$

From the measured spectrum, $\Delta\lambda = 8.57\ nm$ and $\lambda_\circ = 801\ nm$. From this we get a minimum pulse duration of 110 fs, which matches with the specs. However, this assumes that all the modes have the same phase. If there is group velocity dispersion, the pulse duration will spread. To confirm that the pulse is optimally compressed by the Legend, we need a way of directly measure the pulses.

The pulses of our laser system are short enough that photodiodes are not fast enough to measure the duration of the pulses. So in order to get information about the pulse, we need to use the pulse itself to characterize the pulse. To this end I built an autocorrelator.

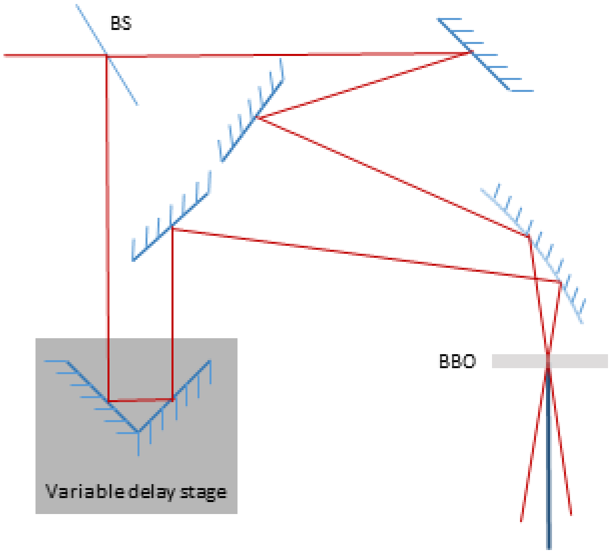

FIG. 4.2: A basic autocorrelator uses divides the pulse into two pathways. Recombining the beams in a BBO crystal will only produce blue light when the pulses overlap both temporally and spatially. By looking at the profile of the blue light we can determine the pulse duration Δt.

An autocorrelator works by splitting the beam into two pathways. These pulses are then recombined in a material with a strong second order process. In our case we use a BBO crystal that has second harmonic generation (SHG). SHG is a two photon process, so at low enough intensities there will be no blue-light generation with a single pulse.

But when second harmonic generation happens with photons from both pulses, there is sufficent intensity to produce a blue spot (400 nm) in-between the two incoming 800 nm beams.

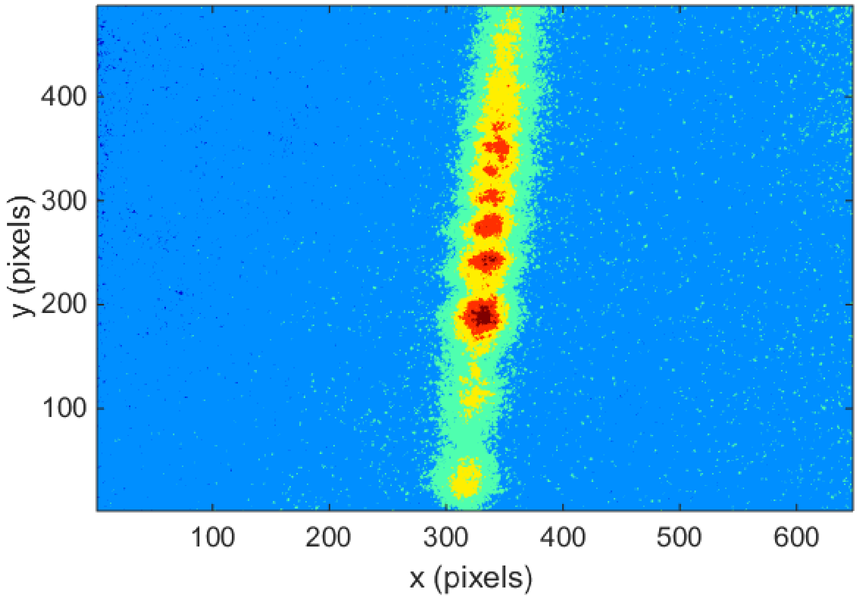

FIG. 4.3: The image from the camera of our autocorrelator shows the SHG from the combination of the two pulses in the BBO crystal. The width of the beam is related to the pulse duration. Each pixel is 7.4 microns.

In order to get the pulse duration δt, we fit the beam with a Gaussian to get the width of the beam. In order to calibrate the autocorrelator, we take an image after changing the length of one of the beam paths with a delay stage. There is a linear relationship between the beam position on the camera and the change in time delay of the pulse. From this we can calculate δt by

$$\delta t = frac\delta x \times msqrt(2) \tag{4.3}$$

where δx is the fitted width of the beam in the horizontal direction, m is the slope of change in time delay over change in beam position. The $sqrt(2)$ is a correction factor based on the assumption that the pulse envelope is Gaussian.

4.3.2 Fluence and Spot size

The Fluence of a beam is defined as the energy of the laser pulse over the area of the beam. If P is the average power of the beam, R is th repetition rate, and w_o is the waist of the beam, we can calculate the fluence by this equation:

$$F = \frac{P}{R \times \pi w_o^2} \tag{4.4}$$

The repetition rate of our laser system is 1kHz, and the waist size depends on the focal length of the lens. We used a camera to measure the spot size of our pump beam. However, the camera we used had a resolution of 7.4 microns per pixel, and was prone to saturate at the focal point. So we took images of the cross-section of the beam at several points after the lens. The focal length of the pump laser is 50 cm.

4.4 Pump-probe set up

The majority of the measurements I made were in a pump probe configuration, as can be seen in figure 8.1. In our set up, a pulse is split with an (20/80) beam-splitter, where the more powerful leg is sent through a variable neutral density filter, allowing us to control the power in the pump pulse. It's focused with a 500 mm lens. The second leg is sent down a variable delay stage (total length of 600 mm) before being further attenuated and focused onto the sample with a 250 mm lens. By changing the path length, we change the amount of time that it takes for the pulse to reach the sample. This allows us a finer time resolution than we could get just from measuring the response from a continuous wave beam.

By changing the distance that the probe pulse travels, we can get a snapshot of the film's response at some Δt from when the pump pulse hits the sample. So at negative

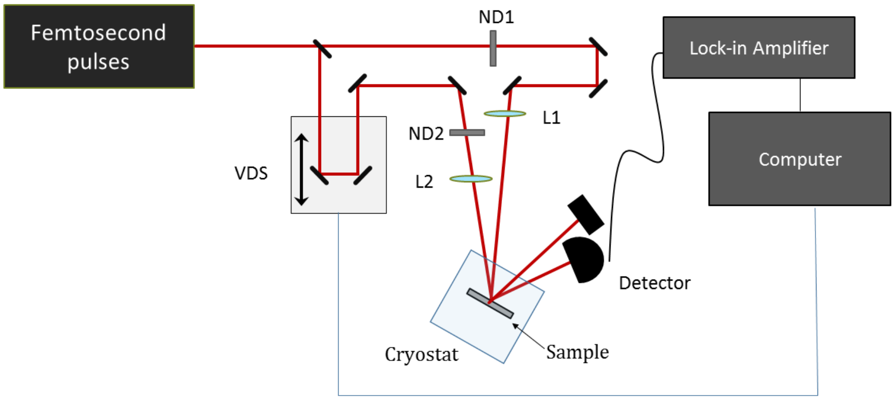

FIG. 4.4: Schematics of the optical pump-probe experimental setup. The output of the amplified ultrafast laser is split into weak probe and strong pump beams using a (20/80) beamsplitter (BS). The energy of the pump pulses is controlled by the variable neutral-density filter ND1, while the probe beam was sent through a computer-controlled variable delay stage (VDS) and further attenuated using ND2 (OD=3.0). The probe and pump beams were focused on the same spot at the surface of the sample, placed inside the cryostat, using 250-mm and 500-mm lenses, correspondingly. The reflected probe power was measured by the photodetector (PD), and further analyzed using a lock-in amplifier.

Δt, the probe is looking at times before the pump hit the sample, and at positive Δt the probe is measuring the sample's reaction to the pump pulse. The delay stage has a range of 600 mm (4 ns) and a step size of 1.25 microns (8 fs). This is a much finer resolution then our pulse length, which means our time resolution is limited by the laser pulses, not the stage.

In all measurements, reported below, the relative change in reflection $\Delta R/R$ is defined as $\frac{R_o - R(\tau)}{R_o}$, where R($\tau$) is the power of the measured reflected probe beam as the function of the delay τ between the pump and the probe pulses, and R_o is the probe reflected power in the absence of the pump beam.

CHAPTER 5

Phase Diagram of Ultrafast Response

5.1 Introduction

Many applications can benefit from the ability to controllably change the electrical and/or optical properties of some materials that can undergo a metal-to-insulator phase transition (MIT). Vanadium dioxide VO_2 has been a model material for many such studies, as it undergoes a reversible thermally-induced MIT at a convenient transition temperature (T_c=340 K for bulk VO_2)[5, 6]. The MIT in VO_2 can also be induced at sub-picosecond timescales using ultrafast optical pulses[43], and also by applying sufficiently strong electric fields.[44]

VO_2 belongs to a class of highly-correlated materials, in which the electrical properties depend on strong electron-electron interactions. The MIT is currently understood to be due to the interplay of strong electron-electron interactions and a change of the VO_2 crystal structure.[23**?** , 45]. For $T<T_c$ VO_2 is insulating and has a monoclinic crystal structure, while for $T>T_c$ it is metallic and as a rutile lattice structure [6]. The lower symmetry of the monoclinic phase is characterized by the dimerization of the V^{+4} ions along the c-axis of the rutile phase[5]. This change in the lattice structure, to which the electron-electron interactions contribute, results in the opening of a band gap in the band structure, illustrated in Fig.2.1. [1]. While a complete description of the transition mechanism has not yet been achieved, it is generally accepted that the MIT in VO_2 is due to the interplay of a Mott-Hubbard electronic instability in which the electron-electron interactions play the critical role, and a Peierls instability of the lattice.[20, 46, 47, 48]

There are numerous potential applications for VO_2.[**?** 49, 50, 29] Implementation of such VO_2-based new technologies requires the ability to tailor the MIT properties to the demands of the particular application. For example, several studies demonstrated that the critical temperature of a thermally-induced MIT can be adjusted by doping VO_2 films, or by applying pressure along the rutile c-axis. [51, 52, 38]. The MIT characteristics also exhibit dependence on the choice of the substrate material. The substrate material can affect the VO_2 thin films characteristics [eg. due to strain]. [9, 10, 11, 12, 13]. In particular, our previous studies have shown significant differences between the MIT critical temperatures for VO_2 samples grown on TiO_2 [011], SiO_2 (quartz) and c-Al_2O_3 under identical deposition conditions [45]. In the experiments reported here, we have focused our investigations to the effects of a substrate (material and microstructure) on the ultra-fast photo-induced MIT in two VO_2 thin film samples, specifically grown on TiO_2 [011] and c-Al_2O_3. For these measurements the MIT was induced by a strong ultrashort (∼100 fs) laser pulse, and the optical properties of the films were probed by a much weaker probe pulse, arriving with a controlled delay. Following the methodology, proposed by Cocker et al.[20], we have observed and mapped out a range of values of the pump laser fluence corresponding to distinct phases of the photo-induced MIT at various sample temperatures. We then analyzed the possible connection between the two film's microstructure and observed differences in MIT dynamics.

5.2 Differences in the VO_2 films structure for different substrates

In these studies we used two VO_2 thin films, produced using the same method (Reactive bias ion target beam deposition [53]) on two different crystalline substrate materials: one 80 nm-thick VO_2 film was grown on a 330 μm c-Al_2O_3 substrate, and the other 110 nm-thick VO_2 film was grown on a 500 μm TiO_2 (011) substrate.

Both VO_2 films were characterized by X-ray diffraction (XRD), as outlined in Ref[7] and Ref[10]. The XRD measurements of the sample grown on Al_2O_3 substrate show the film orientation in the (020) direction with six-fold in-plane symmetry, corresponding to three possible orientations of the VO_2 grains within the film. The VO_2 film grown on TiO_2 substrate exhibits a mono-crystalline structure, with a single XRD peak corresponding to a highly-strained monoclinic structure approaching a rutile (011) plane. Such high degree of strain is due to the larger lattice constant of TiO_2 substrate resulting in clamping of epitaxial VO_2 films[10, 21].

Unsurprisingly, these structural differences have an effect on the characteristics of the thermo-induced MIT[45]. Namely, the MIT at the VO_2/Al_2O_3 sample occurred at higher transition temperature (T_c=341 K) and had broader width (T_c=26 K), compared to the VO_2/TiO_2 (T_c= 310 K, T_c=9 K). This is possibly due to a wider distribution of grain sizes and strain in the film that has been observed in similar samples in previous papers.[45, 24, 25, 54].

We measured the DC conductivity with applying a 4-point probe technique and found the DC conductivity of VO_2 on Al_2O_3 at 370 K to be 2.24×10^5 S/m, while the DC conductivity of VO_2 on TiO_2 at 340 K was found to be 3.03×10^5 S/m. We also evaluated the penetration depth at 800 nm for both films. For the film grown on Al_2O_3 we looked at the reflection and transmission with a cw laser, which gave us a penetration depth of $\delta = 294$ nm, where $I = I_o \times 10^{-x/\delta}$. The TiO_2 substrate did not have a polished backside, so we used ellipsometry to measure its optical constants at a range of wavelengths between 420 nm to 749 nm. We took this data and extrapolated to get the real and imaginary parts of the optical constants, and determined a penetration depth at 800 nm optical wavelength to be $\delta = 255$ nm.

5.3 Experimental Apparatus

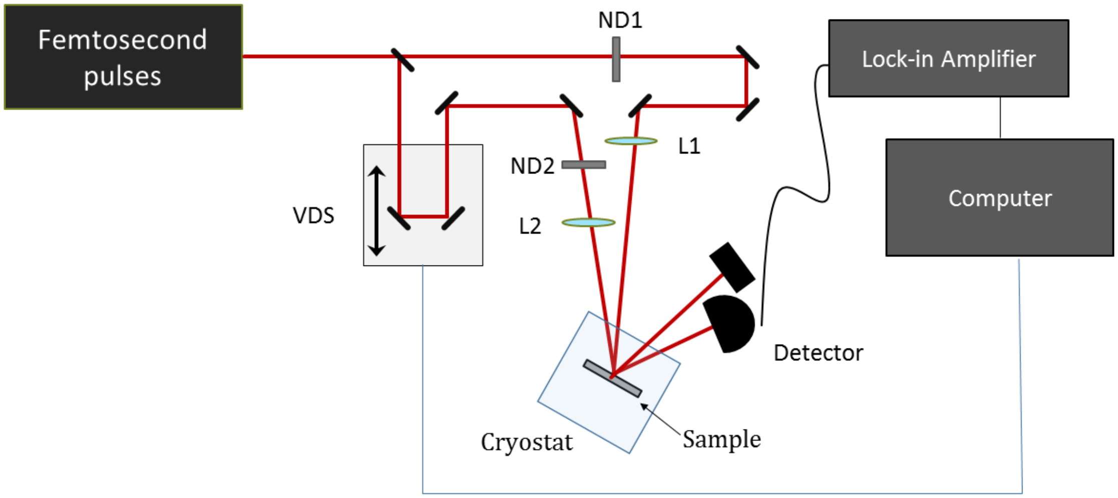

FIG. 5.1: Schematics of the optical pump-probe experimental setup. The output of the amplified ultrafast laser is split into weak probe and strong pump beams using a (20/80) beamsplitter (BS). The energy of the pump pulses is controlled by the variable neutral-density filter ND1, while the probe beam was sent through a computer-controlled variable delay stage (VDS) and further attenuated using ND2 (OD=3.0). The probe and pump beams were focused on the same spot at the surface of the sample, placed inside the cryostat, using 250-mm and 500-mm lenses, correspondingly. The reflected probe power was measured by the photodetector (PD), and further analyzed using a lock-in amplifier.

In all measurements, reported below, the relative change in reflection $\Delta R/R$ is defined as $\frac{R_o - R(\tau)}{R_o}$, where R($\tau$) is the power of the measured reflected probe beam as the function of the delay τ between the pump and the probe pulses, and R_o is the probe reflected power in the absence of the pump beam.

5.4 Measurements of the MIT Temporal Evolution

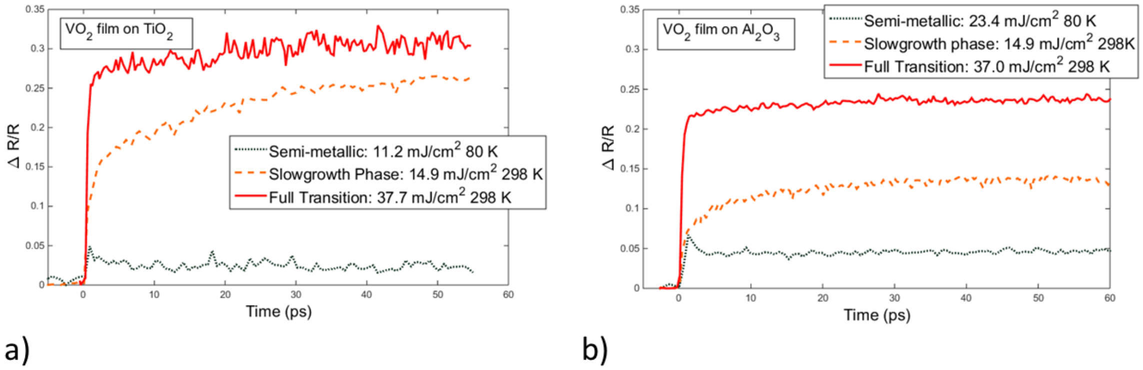

FIG. 5.2: Sample time-dependent changes in the probe reflection corresponding to various dynamical phases of MIT, measured for (a) VO_2/TiO_2 and (b) VO_2/Al_2O_2 samples. The pump pulse hits the sample at zero time, and positive delay times correspond to the probe beam interacting with the sample after the pump beam.

Overall, the temporal evolution of the photo-induced transition in both samples followed similar trends, as illustrated in Fig. 5.2. We varied the pump pulse energy and the temperature we held the sample, keeping the initial temperature well below the T_c. For both films we observed three distinctive dynamical MIT regimes. Similar behavior has been previously reported by Cocker et al[20] in their studies of the THz probe transmission evolution in a photo-induced MIT in a VO_2 film deposited on Al_2O_3. At sufficiently high fluences, we observed a very fast (< 1 ps) change of the probe reflectivity from the value corresponding to the insulating VO_2 state to the fully metallic VO_2 state, that implies that the whole VO_2 films quickly transitioned from the insulating to the fully metallic state (âĂIJfull-MITâĂİ phase). We characterize the minimum pump fluence value required to achieve this full transition as $\Phi_{full-MIT}$. For intermediate values of the pump fluence

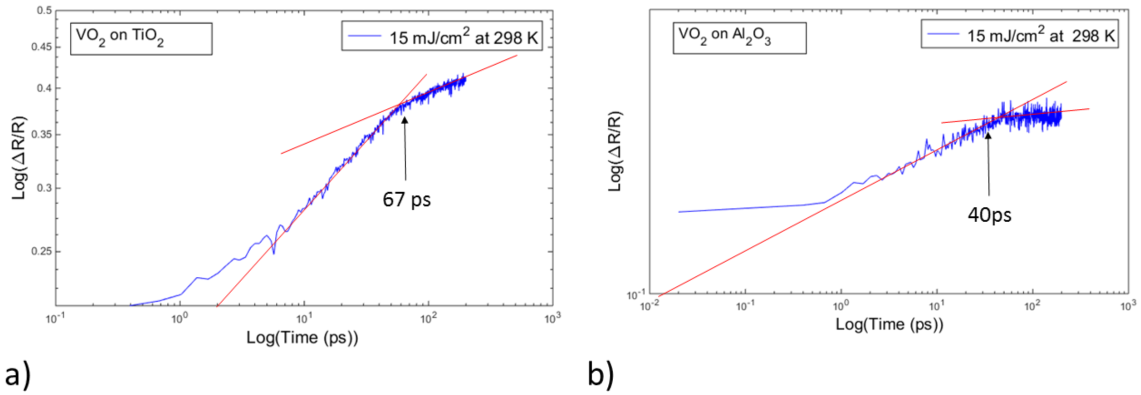

FIG. 5.3: âĂIJSlow growthâĂİ of relative reflectivity with time, measured for (a) VO_2/TiO_2 and (b) VO_2/Al_2O_2 samples with pump fluence of 15 mJ/cm^2 at 298 K, using a log-log scale (âĂIJslow growthâĂİ phase data in Fig.5.2. Log-log scale clearly shows two time scales of growth for both films. For the VO_2/Al_2O_3 sample, the initial faster reflectivity growth (time constant 7.4± 0.3 ps) for the first 40 ps was followed by much slower growth with time constant of 33± 8 ps. For the VO_2/TiO_2 film the switch occurred at approximately 67 ps, from the time constant 6.3±0.2 ps to 15.0± 0.6 ps.

below $\Phi_{full-MIT}$, the film reflectivity also changed immediately after the pump pulse, but this change did not reach the value corresponding to the fully metallic VO_2, implying that the resulting state of the film contains both metallic and insulating regions. Moreover, after this initial sub-picosecond change the relative reflectivity continued to grow at a much slower rate for a few hundreds of ps ("slow growth" phase), indicating further coarsening of the metallic component of the VO_2 film. Interestingly, this dynamical behavior is consistent with the slow coarsening of metallic puddles within the insulating matrix, observed in the thermo-induced MIT.[55, 56, 57] Fig. 5.3 shows the change in both samples reflectivity $\Delta R/R$ at 15 mJ/cm^2 on a Log-Log scale to characterize the rate of this evolution more clearly. It is easy to see the two distinct time constants of this slow growth for both films, with two distinct switching times. In general, rate of slow growth decreased at the lower

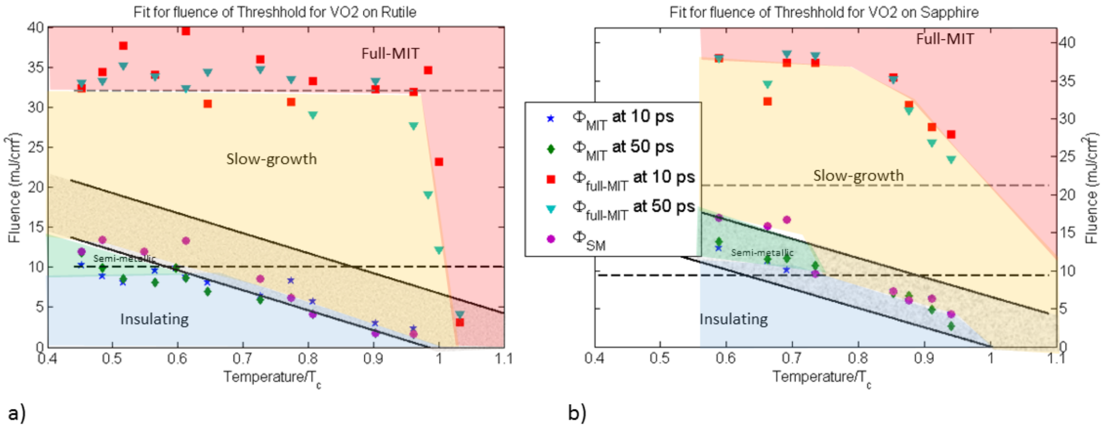

FIG. 5.4: Threshold measurements for the onset and for the full MIT of VO_2 thin films grown on a)TiO_2 and b)Al_2O_3. Blue stars/Green diamonds correspond to the threshold fluence needed to see a 2% rise in reflectivity at 10 ps and 50 ps, correspondingly. The red squares and cyan triangles correspond to the fluence required to reach the reflectivity value for a fully metallic film in the first 10 ps and 50 ps, correspondingly. The purple circles indicate the boundary where the âĂŹslow-growthâĂŹ phase starts Φ_{SM}. To define this boundary, we took several measurements of the probe reflectivity $\Delta R/R$ as a function of time for the first 20 ps at a range of pump fluences, fitted their linear slopes, and then found fluence values at which the slope becomes indistinguishable from zero within the measurement uncertainty. The dashed lines are the calculated photo-excited electron densities at the front and the back of the films. The shaded region between the solid lines is calculated fluence needed to bring the films up to the transition temperature.

values of the pump fluence.

At lower values of the pump fluences, the time evolution of the film became dependent on the temperature of the sample. At higher temperatures if the pump fluences is insufficient to reach the slow growth regime, the reflectivity of the sample after the first few ps returned to its insulating value, indicating no long-term changes in the VO_2 state. However, at the lower temperatures (below 250 K for VO_2/Al_2O_3 and below 220 K for VO_2/TiO_2) we clearly observed an intermediate “semi-metallic” phase, as shown in Fig 5.2. For this regime, which occurs at lower fluences than the slowgrowth phase, the pump pulse induced the initial few percent change in relative reflectivity, but then it remained constant, implying no further changes in the VO_2 film phase distribution. While we observed a qualitatively similar photo-induced MIT dynamics for the two VO_2 films grown on TiO_2 and on Al_2O_3 substrates, the structural differences between the two films clearly affected the experimental conditions for realization of each MIT phases. To highlight these differences, Fig. 5.4 shows the experimentally measured values of the fluence thresholds between the phases: $\Phi_{full-MIT}$, the fluence required to induce a fast full transition to the metallic stage; Φ_{SM}, the fluence sufficient to induce the partial MIT, followed by the slow growth of the metallic component; and Φ_{MIT}, the minimum pump fluence required to produce any phase transition in the insulating VO_2 film. For consistency each threshold value was measured for 10 ps and 50 ps delay between the pump and the probe pulses. Also, to take into account the difference between the critical temperatures for the two VO_2 samples, for the phase diagram in Fig. 5.4 we used the relative temperature T/T_c for each sample.

The most noticeable difference between the two samples was observed in the temperature dependence of the full-MIT threshold $\Phi_{full-MIT}$. For the VO_2 film on Al_2O_3 the values of $\Phi_{full-MIT}$ increased slowly as the sample temperature dropped. At the same time, for the VO_2/TiO_2 sample the entire full MIT boundary $\Phi_{full-MIT}$ remained constant for all the temperatures $T/T_c < 0.95$, after the sharp drop around T_c. Remarkably, the measure values for in the two samples were rather similar (around 32-34 mJ/cm^2 for $T/T_c \sim 0.6$) despite their structural differences of the films.

The other two threshold values, corresponding to a partial MIT displayed similar temperature dependences for both samples: at lower sample temperatures it required higher pump power to induce the same change in the sample. However, the exact values for Φ_{MIT} and Φ_{SM} were higher for the VO_2/ Al_2O_3 sample. We also observed the separation of the slow-growth phase and the semi-metallic phase for temperatures below $T/T_c \leq 0.7$ for the both films.

It is important to note that the MIT dynamics for VO_2/Al_2O_3 sample observed in the current experiment using all-optical pump-probe detection, was qualitatively similar to that for a similar VO_2/Al_2O_3 sample studied by Cocker et al.[20] using 800 nm optical pump pulses and broadband THz probe pulses. Their reported values for threshold fluences were 2-3 times lower than those shown here in Fig. 5.4. However, other works have shown higher threshold values for the onset of MIT, around 7 mJ/cm^2, and show comparable behavior at higher fluences. [19**?**]

5.5 Mechanisms of Ultrafast MIT

Accurate theoretical description of the fast dynamics of the electron system in VO_2 is a very challenging problem. It requires a proper description of the strong electron-phonon coupling and of the strong electron-electron correlations in the insulating phase, and of the interplay between these correlations and the lattice structure dynamics. However, the analysis of the experimentally measured time evolution of the VO_2 reflectivity after the pump pulse may allow us to infer qualitatively the dominant processes that govern the dynamics in the VO_2 films that we have studied and, in particular, how these processes differ between VO_2 films deposited on TiO_2 and on Al_2O_3.

After the pump pulse the reflectivity, $\Delta R/R$, of the VO_2 film, that is initially in the insulating phase, increases on a very short time scale[47], shorter than our time resolution ~ 0.5 ps, as shown in Fig. 5.2. The change in reflectivity soon after the pump pulse was shown to be directly proportional to the pump fluence,[47] and therefore can be attributed to the almost instantaneous excitation of electrons from the valence band to the conduction band of the monoclinic phase of VO_2 by the pump pulse.

As shown clearly in Fig. 5.2, and described in the previous section, the behavior on time scales longer than 1 ps strongly depends on the pump fluence and the temperature of the sample[20].

For sufficiently high values of the fluence $\Phi \geq \Phi_{full-MIT}$, the reflectivity increased to the values matching that of the fully metallic VO_2 film[45]. This indicates that for this regime the population of electron-hole excitations created by the pump pulse was large enough to cause a structural deformation[47, 58] throughout the whole VO_2 film and nearly instantaneously drove it from the monoclinic to the rutile phase. The rutile phase is metallic and therefore the excited electrons have no states in the valence band to which they can decay to. For this reason, the film remains metallic until the lattice cools down to temperatures below T_c causing the reversed transition from rutile to monoclinic. This relaxation process is slow and takes place on time scales much longer (> a few ns) than the time interval (few hundred ps) considered in this experiment.

In the limit of weak pump pulses (below a threshold value Φ_{MIT}), the observed change in reflectivity did not last much beyond the duration of the pump pulse, quickly returning to its original value. This can be attributed to the fast relaxation of the particle-hole excitations created by the pump laser: since the number of electron-hole excitations is not high enough to induce a coherent lattice deformation and to drive a noticeable fraction of the VO_2 film from the monoclinic insulating phase to the rutile metallic phase, electrons decay quickly from the conduction to the valence band of the monoclinic structure, quickly restoring the original value of the measured reflectivity.

The time evolution of the reflectivity is more complex at intermediate values of the fluence $\Phi_{MIT} < \Phi < \Phi_{full-MIT}$. For these values, the reflectivity kept increasing after the almost instantaneous step. We attribute this behavior to the fact that for $\Phi_{MIT} < \Phi < \Phi_{full-MIT}$ the population of electron-hole excitations created by the pump pulse is large enough to trigger the coherent structural deformation that drives the lattice from the monoclinic phase to the rutile phase in some regions of the sample but not in the whole sample. The rutile regions initially form, then heat up the surrounding monoclinic regions and drive them to the rutile phase, as well. This process leads to coarsening of the metallic regions, and may be responsible for the observed continuing increase of the reflectivity on time scales of the order of tens of picoseconds. It also may explain the existence of two timescales in the slow growth regime, shown in Fig. 5.3: at shorter times the change in reflectivity can be dominated by lattice vibrations that can persist up to 100 ps after the initial pump pulse excitation[38]. At later times, heat diffusion mechanisms dominate the transition dynamics.

In this model we expect the values of Φ_{MIT} to decreases as the sample temperature approaches the critical temperature of the thermo-induced transition, since a lower number of electron-hole excitations is necessary to drive the structural phase transition. It is also expected that the semi-metallic phase should appear at the lower temperatures ($T/T_c < 0.7$ for both samples) and lower pump fluences $\Phi_{MIT} < \Phi < \Phi_{SM}$, corresponding to a situation in which the power is sufficient to trigger the MIT transition in isolated regions, but not enough to induce the growth of the metallic regions to the rest of the sample.

We now discuss how the measured structural differences between the two VO_2 films may affect the dynamics of the photo-induced MIT. The large measured strain induced by the TiO_2 substrate indicates that the equilibrium monoclinic VO_2 film is already de-formed toward rutile structure, thus making the structural transition easier. This, and the more ordered mono-crystalline structure of the VO_2/TiO_2 samples seems to favor the formation of the more uniform nucleation sites during MIT, as evident by a the narrower thermally-induced MIT in this sample, happening at lower critical temperature. The significantly broader width of the MIT transition in the VO_2/Al_2O_3 sample implies the broader distribution[24] of the metallic nucleation cluster sizes compared to VO_2/TiO_2 samples, as the connection between the width of the thermally-induced MIT and the structure of the film have been demonstrated previously.[45, 24, 25, 54]

These structural differences may also play a critical role in explaining the observed differences in temperature dependence of the full MIT threshold $\Phi_{full-MIT}$ for the two samples. The absence of the temperature sensitivity of $\Phi_{full-MIT}$ for VO_2/TiO_2 sample indicates that once the critical density of the photo-electrons is reached, the whole film undergoes the MIT uniformly, independently of its original temperature. While there is no direct proof, this observation is consistent with a more strained and more ordered monocrystalline structure of the sample, as well as the sharper thermally-induced MIT transition. In contrast, the less ordered structure of the VO_2/Al_2O_3 sample may give rise to stronger local variations of the critical temperature throughout the sample (as indicated by a much wider thermally-induced MIT transition). This non-uniformity can then be reflected in stronger local variations in the critical density of particle-hole excitations necessary to induce the coherent lattice distortion and to drive the structural transition, resulting in the critical density of electron-hole excitations necessary to drive the full MIT in the whole sample to be temperature-dependent.

We can attempt to estimate the minimum pump fluence values required to excite the critical density of photoelectrons to match the free electron density in the metallic phase of the VO_2 film in equilibrium (above the critical temperature). First, we estimate the electron density in the metallic VO_2 films from the measured dc electrical conductivity, using the Drude-Smith model[59]:

$$\sigma_{DC} = \frac{ne^2\tau_{DS}}{m^*} \times (1+c) \tag{5.1}$$

where n is the electron density, τ_{DS} is the scattering time, $m*$ is the effective mass of the electrons, and c is the correlation parameter, such that $c = 0$ corresponds to free Drude electrons, and $c = -1$ corresponds to fully localized electrons. Using the previously established values for τ_{DS}, m, and c,[59] the estimated value of electron densities are $3.2 \times 10^{21}\text{cm}^{-3}$ for the VO_2/TiO_2 sample, and $2.35 \times 10^{21}\text{cm}^{-3}$ for the VO_2/Al_2O_3 sample.

Second, we approximate the number of photo-electrons by the number of photons absorbed; although in this way we clearly overestimate the photoelectron density, this provides an order of magnitude estimates of the required fluences. Following a similar procedure, described in Ref.[9], we compute the values of the MIT thresholds Φ_{MIT} and $\Phi_{full-MIT}$ based on reaching the critical density of the photoelectrons at the front of the film (using full pump laser fluence) and in the back of the film (using the attenuated pump laser fluence due to reflection and absorption inside the film). Using the measured values of the penetration depth of the 800-nm optical beam, we estimated the threshold fluence needed to photo-excite the metallic electron density at the front of the VO_2/TiO_2 film to be approximately 10 mJ/cm^2, and the fluence required to excite the metallic electron density at the back of the film to be 36 mJ/cm^2. These values are shown as dashed horizontal lines in Fig. 5.4(a). The higher threshold matches the boundary measured for the full metal-insulator transition. Analogous calculations for the VO_2 film on Al_2O_3 lead to threshold fluence values of 9.3 mJ/cm^2 and 21 mJ/cm^2, respectively. We can see that for Al_2O_3 both thresholds obtained in this way do not match the Φ_{MIT} and $\Phi_{full-MIT}$ thresholds obtained experimentally.

Finally, we roughly estimated the minimum pump fluence values required to heat the

VO_2 films to the thermally-induced phase transition, assuming that all the absorbed optical energy was eventually transferred to heating the sample. The two solid lines in Fig. 5.4 are due to the finite width of the MIT, as can be seen in Table 5.5. The lower solid lines correspond to the minimum pump fluence required to increase the sample temperature to the beginning stage of the thermally-induced MIT (specifically to T=305 K for the VO_2/TiO_2 sample, and T_c = 325 K for the VO_2/Al_2O_3 sample). The upper lines assumed that the samples reached the fully metallic phase at T=315 K and T=355 K respectively, and included the latent heat required for the phase transition. In these estimates we used the value of heat capacity of the VO_2 film to be 3.0 J/cm^3 K, and the latent heat of 235 J/cm^3.[60] For both films we find that the experimental Φ_{MIT} threshold matches semi-quantitatively the threshold obtained by estimating the value of the fluence needed to raise the temperature of the VO_2 film to T_c.

	Film grown on TiO_2	Film grown on Al_2O_3
Average VO_2 grain size (from XRD)	Out of plane: >13 nm	Out of plane: 45 nm
VO_2 film thickness	110 nm	80 nm
Thermal Transition Temperature T_c	310 K	340 K
MIT width ΔT_c	9 K	26 K
DC Conductivity	at 297 K 7.01×10^3 at 340 K 3.03×10^5	at 296K 1.71×10^2 at 369 K 2.24×10^5
Penetration depth at 800 nm	255 nm	294 nm
Slowgrowth threshold fluence Φ_{MIT}	1.2 mJ/cm^2 at 300 K 4.2 mJ/cm^2 at 250 K 13.3 mJ/cm^2 at 190 K	6.1 mJ/cm^2 at 300 K 10.6 mJ/cm^2 at 250 K 16.7 mJ/cm^2 at 200 K
Pump fluence required induce the full transition	27.8 mJ/cm^2 at 300 K 33.4 mJ/cm^2 at 250 K 32.4 mJ/cm^2 at 190 K	31.9 mJ/cm^2 at 300 K 37.4 mJ/cm^2 at 250 K 37.9 mJ/cm^2 at 190 K
Semi-metallic stage emergence conditions	8.5 mJ/cm^2 at 220 K	12 mJ/cm^2 at 250 K

TABLE 5.1: Summary of basic properties of the two VO_2 samples.

5.6 Conclusion

In conclusion, we have investigated the role of substrate-induced microstructure on the ultrafast dynamics of the photoinduced metal-insulator transition in VO_2 films, using optical pump-probe techniques. In particular, we have identified the characteristic patterns of the MIT dynamics that depend on pump laser energy and the temperature of the film, and measured the threshold pump fluence values that characterize the onset and full MIT between such behaviors. We found that two VO_2 samples - one grown on sapphire substrate, and the other grown on rutile substrate, require rather similar threshold laser fluence values, despite a rather significant (30 K) difference in the critical temperature for the thermally-induced MIT. We also identified several important differences, summarized in Table 1. In particular, for the VO_2 film on TiO_2 we found almost no temperature dependence in the values of fluence threshold for the full MIT, while for the VO_2/Al_2O_3 sample this threshold clearly decreased as T approaches T_c. This difference may be linked to the large lattice strain and differences in width of the thermo-induced transition, which we suspect is linked to the variance of the grain size of the film. Understanding the changes in the transition dynamics of films on difference substrates will potentially allow for the selection of desirable traits in the MIT, which is important for future VO_2-based technologies.

CHAPTER 6

VO_2 sub-picosecond polarization dependent response

6.1 Sub-picosecond response

Right after the pump hit VO_2, $\Delta R/R$ shows an interesting response depending on the relative orientation of the polarization of the pulses. When the probe and the pump have the same polarization, there emerges a quick feature that has a width of ~200 fs. This is independent of the orientation of the films in relation to the polarization of the pump and probe. I have seen this both on the films grown on Al_2O_3 and TiO_2. Figure 6.1 shows this sub-ps feature, as measured with the VO_2 on TiO_2. As can be seen, when we have the two beams cross-polarized we see a response in the signal whose timescale is proportional to the duration of the pump pulse, and there is no sub-ps feature. When the two beams are parallel the sub-ps feature occurs while the pump hits the sample, but does not scale with the duration of the pump (Δt). For shorter Δt, the feature becomes more difficult to see, as the underlying response to the pump cuts off the sub-ps feature. There is currently no

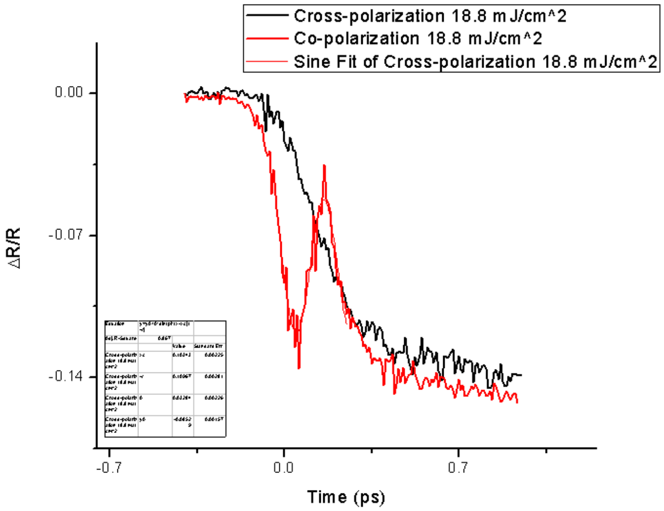

FIG. 6.1: This is a measurement taken with the sample of VO_2 on TiO_2. The sub-ps feature can be clearly seen in this graph when the pump and probe are cross polarized.

observation of this in the existing literature.

The obvious thought is that we are seeing an interference pattern from reflections off the back of the samples. A few things lead us to believe this is not the case. The pump and probe come at the sample from two different directions, and the majority of the pump in reflected in a different direction. It's possible that there is some scattered pump that is interfering with the probe, but this is negated by the fact that the feature disappears when we do a pump-probe measurement with the film heated to the metallic state.

There are two plausible explanations for this dip in reflectivity that we are seeing: we could be seeing a strong oscillation from the lattice, or there could be a plasmonic response in the film. The lack of dependence on the lattice orientation would suggest that it is a plasmonic response. However the width of the feature is 142 ± 8 fs,which corresponds to a frequency of 7.0 ± 0.4 THz, which could be one of the Raman modes we measured in Chapter 3. I have tried several different methods to try to determine which of theses mechanisms is happening in our VO_2 thin films. First I tries applying a strong magnetic field on the films while preforming the pump-probe. I then investigated changing the polarization of the incoming beams. Finally, I got the most interesting results in looking at changing Δt of the incoming pulses.

6.2 Electromagnetic Field

I used a GMW Dipole electric magnet, to produce a magnetic field. The strength of the magnetic field produced is dependent on the current and the geometry of the poles of the electromagnet(size of pole ends and separation). Because of the mount I used for the film, I had a separation of 4 cm, which limited the magnetic field I was capable of getting. Another limitation is the amount of current that I could safely put into the system. I used air to cool the magnet, meaning that I could only safely go up to 2 Amps. I had a Range of 0-1 kGauss.

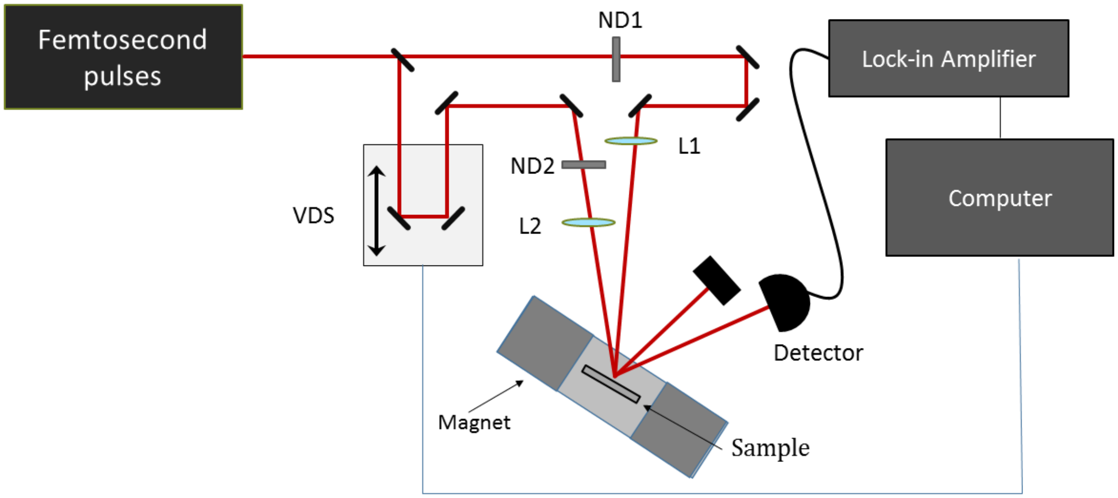

FIG. 6.2: The experimental set up we used for these measurements were much the same as the basic pump-probe measurements, except the sample was not mounted in a cryostat, and there is an electromagnet that creates a magnetic field parallel to the sample surface.

I first looked at the heat-induced insulator-metal transition with a magnetic field, but there was no difference between the having the magnetic field on or off with any of the films. Unsurprisingly, there was also no difference between having a magnetic field on the sample for the pump-probe measurements as well, neither in the sub-ps scale, nor on the long term.

There are a couple different reasons that the magnetic field had no noticeable effect on $\Delta R\ R$. First of all, the magnetic fields I used were very small due to the configuration I chose, and the cooling method I used. In addition to that, the orientation of the magnetic field with respect to the surface was not ideal if we wished to have an effect on a plasmonic resonance. The E-field of the incident beam is parallel to the surface for p-polarized light, and s-polarized light...

6.3 Changing Δt

The other experiment I tried to examine this phenomenon, which had much more interesting results, was to change the pulse duration of our beams. This was easily achieved by adjusting the compression of the pulse within our amplifier. Δt was measured with the autocorrelator, as described in Chapter 4. I took a series of measurements from 130 fs to 1 ps, where at each orientation I measured the trace with co-polarized light and cross-polarized light.

On the left column of Figure 6.3, we see both the cross-polarized measurements and the co-polarized measurements. The right column shows the cross-polarized measurement subtracted from the co-polarized measurement. Figure 6.3 shows that as we increase Δt the cross-polarized response in the sub-ps regime is longer and longer. But when we look at the co-polarized measurements, while the underlying response is the same as the cross-polarized response, the sub-ps feature is unchanged as Δt changes. This is further

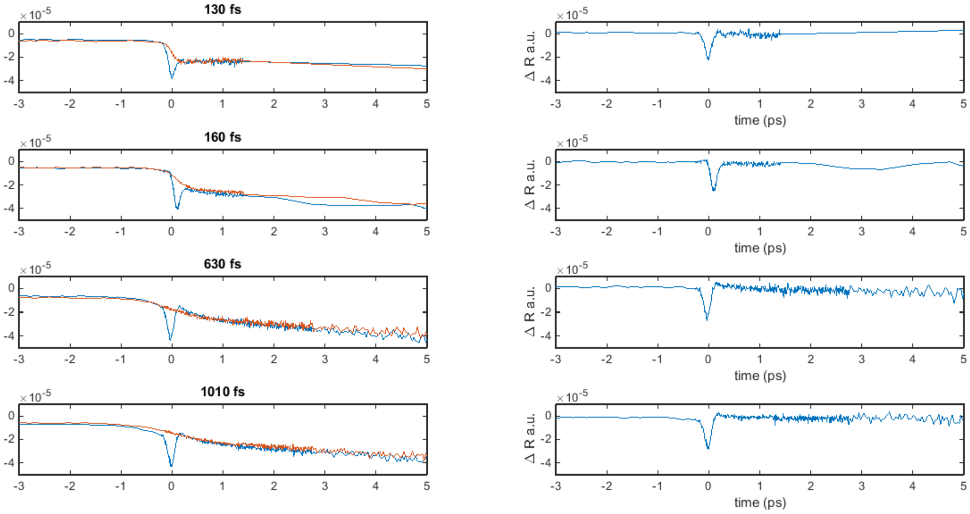

FIG. 6.3: Here are a series of measurements of VO_2 in the pump-probe configuration. The pulse length (as measured with an autocorrelator) goes from 130 fs to 1 ps. The length in the pulse changes how quickly the film responds when the pump and the probe have the same polarization. However, when the pump and probe are cross-polarized there is a ~200 fs feature that does not depend on the pulse length.

highlighted in the right column of graphs, where the feature pops after the subtraction. To the eye, the feature looks the same for all pulse durations, and this is confirmed by fitting them with a Gaussian curve. For this sample the feature has a $1/e^2$ width of 142 ± 8 fs. If we assume this is half of an oscillation, this corresponds to a frequency of 3.5 ± 0.2 THz.

I've also done similar measurements on our VO_2 sample on TiO_2. Again, the feature seems to stay pretty consistent when changing other parameters, but it is narrower than the feature on the Al_2O_3 sample, with a width of 92 ± 8 fs (5.3 ± 0.5 THz).

The other parameter I explored is the intensity of the pump pulse. Figure 6.4 a) shows how the feature gets deeper as we increase the intensity of the pump. The relationship is linear, even when we start to get the the fluences where $\Delta R/R$ starts to saturate, around 30 mJ/cm^2.

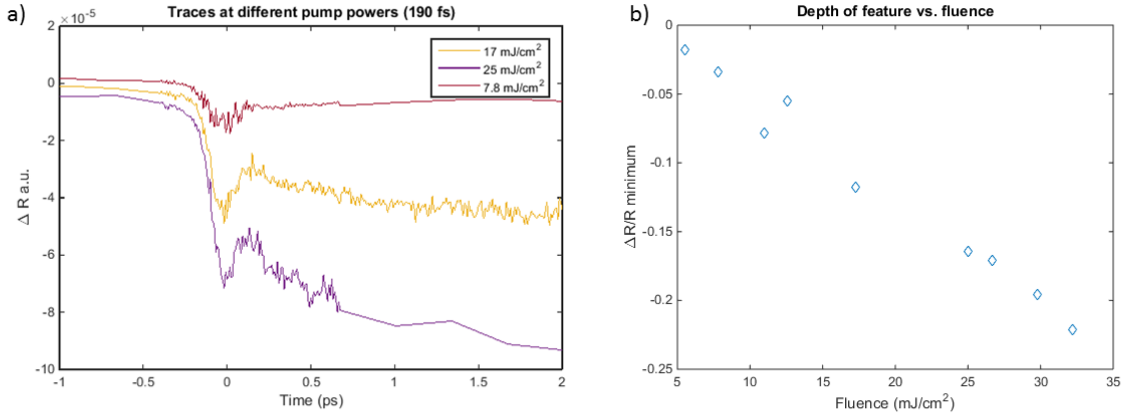

FIG. 6.4: This graph shows the relationship between the intensity of the pump, and the depth of the sub-ps feature. a) Shows the measurement for three different fluences, and one can see a decrease in $\Delta R/R$ for the higher fluence. b) shows the peak of sub-ps feature as a relationship with the fluence.

6.4 Analysis and Conclusion

While I believe these results are interesting enough to include in this work, I do not believe that I have solid enough results to make any conclusions as to what the mechanism behind this feature is. The magnetic field experiments certainly need a higher magnetic field, so I'm loath to make any conclusion from the negative results.

If we look at the timing of the feature, it is not surprising, but it is interesting that our two samples, Vo_2 on TiO_2 and VO_2 show have features with different widths. It is tempting to ascribe them to phonon modes, but they both fall a bit short in energy to any of the known Raman and IR modes. Another argument against the sub-ps feature being a phonon osscillation is the scaling in intensity with the fluence of the pump. I would expect there to be an increase in the restoring force for the ions as we increase the oscillation amplitude, there should be a leveling off of the intensity of the sub-ps feature and eventual saturation.

Another arguement that we're seeing a plasmonic response is that we see this phenomenon both in the more highly crystalline TiO_2 sample and in the more granular Al_2O_3 sample. We are far more likely to see a coherent crystalline response in the TiO_2 sample because it is monocrystalline. In addition to that, I have seen no preference for how the film is orented with relation to the polarization of the beams. What matters is the relative polarization of the pump and the probe.

While theses results are inconclusive, I do believe we are seeing a real phenomenon, and warrent further study. If we can isolate the control of this feature, it opens up possibilities for ultrafast switches that can recover back to the insulating state as fast as it can b triggered to the metallic state.

CHAPTER 7

Decay from metallic to insulating state

One of the difficulties in designing an ultrafast switch is that while the transition to the metallic phase can be quickly stimulated, the relaxation back to the insulating phase happens thermally and takes a much longer time. In order for VO_2 to be feasible as a ultrafast switch, it needs to switch in both directions quickly. There is a difference in how different films of VO_2 on different substrates relax back to M-VO_2. We looked at the film grown on Al_2O_3 and TiO_2, and the dynamics of the relaxation time are very different for these two samples.

As discussed in [61, 62]

Several works [63, 17, 47, 19, 64, 37, 65, 20, 66, 67] have investigated the short timescale dynamics after the photoinduced transition. In particular, Ref. [68] presented a comparison of the long time-scale recovery dynamics between VO_2 films on a crystal substrate or a glass substrate and found that the recovery time for the films on the glass substrate was much longer than for the films on a crystal substrate. The recovery time was modeled using the heat equation to describe the heat flow across the interface between the VO_2 film and the substrate. The difference in the characteristic time between the two types of substrates was attributed to the fact that the thermal conductivity of the interface was expected to be much smaller for glass substrates than for crystal substrates.

In this chapter, we present a theory to properly take into account the effect of inhomogeneities on the recovery dynamics of VO_2 films. Our theory describes simultaneously: (i) the profile of the reflectivity across a thermal induced MIT; (ii) the long time-scale recovery dynamics of the reflectivity after a photoinduced insulator-to-metal transition; (iii) the observed difference of two orders of magnitude between samples with different substrates. Inhomogeneities are due to the fact that the film is comprised of grains with different sizes and different local properties, such as strain [54, 24] and chemical composition.

The presence of inhomogeneities induces a distribution of values for the transition temperature Tc within the film. To take this into account, we derive a generalized heat equation that includes the fact that during the recovery from the photoinduced insulator-to-metal transition, at any given time, a fraction of the sample is undergoing the metal-to-insulator transition, another fraction is still cooling in the metallic phase, and another fraction is already cooling in the insulating phase. A key ingredient of the generalized heat equation is the correct description of the time evolution of the fraction of the sample that is metallic, insulating, or undergoing the phase transition. We then use our theoretical model to obtain the scaling relation between the characteristic recovery time τ and the parameters of the films. Our theoretical model, and the underlying assumptions, are strongly supported by our experimental results. Differently than in Ref. [68], our VO_2 films have all crystal substrates, no glass. Yet, we find that τ can be more than two orders of magnitude different depending on the crystal substrate, TiO_2 or Al_2O_3, Fig. 7.1.

The generalized heat equation (9), which properly takes into account the effect of the films inhomogeneities on the recovery dynamics, is the main result of our work. Our theory allows the description of the recovery dynamics consistently with the measurements obtained for the thermally driven MIT. The scaling between the characteristic recovery time τ and the parameters of the film is another important result of our work.

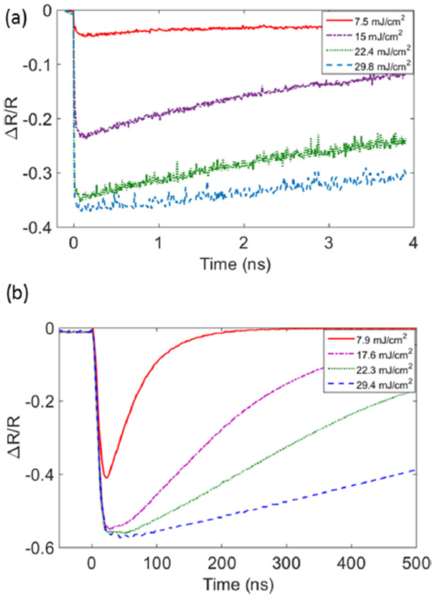

FIG. 7.1: Relative change in reflectivity(R/R) for the VO_2 film on (a) Al_2O_3 substrate and (b) TiO_2 substrate as a function of time after the MIT is induced at time t = 0 by a strong ultrafast pump pulse. The values of the pump fluence are shown in the legend, and the sample temperature is set to (a) 311 K and (b) 280 K, which correspond to approximately 30 K below the critical temperature T_c for thermally induced MIT for each sample.

Our work is relevant to the more general problem of how spatial inhomogeneities affect a first-order phase transition. The ability of our treatment to contribute to this general problem relies on the fact that in VO_2 the two phases across the first-order phase transition have very different electronic properties (metallic versus insulating behavior) that allows us to get an accurate phase mapping, via optical reflectivity measurement, of the time evolution of the metallic (insulating) fraction and, indirectly, of the spatial inhomogeneities present during the transition.

The work is organized as follows. Section II describes the experimental arrangements to measure the optical reflectivity time evolution. The details of the theoretical model that we use to characterize the distribution of the filmsâĂŹ inhomogeneities and the long-time dynamics of the reflectivity after a photoinduced insulator-to-metal transition are presented in Secs. III and IV, respectively. In Sec. V, we demonstrate how the variations in statistical properties of the two films result in a significant difference in the relaxation time scales, and in Sec. VI, we provide our conclusions.

7.1 Experimental Set-up

In our experiments, we studied two VO_2 thin-film samples, both of which were produced using reactive-bias target ion beam deposition (RBTIBD) [38]. One sample was grown on 0.5-mm-thick c-Al_2O_3, and the thickness of the VO_2 film was 80 nm. The other sample was grown on a 0.5-mm-thick TiO_2 (011) substrate, and was measured to be 110-nm thick. Xray diffraction (XRD) evaluation of both films showed them to be crystalline, and detailed characterization information is available in previous reports [49, 45].

For the photoinduced insulator-to-metal transition experiments, we used an ultrafast laser system (Coherent Mantis oscillator and Legend Elite regenerative amplifier) with approximately 100-fs pulses with a central wavelength at 800 nm and a repetition rate of 1 kHz. The properly attenuated output of the laser was split into strong pump pulses and weaker probe pulses using a beam splitter in a standard pump-probe configuration, shown in Chapter 4. The more powerful pump beam, focused to a 180-Îijm-diameter spot on the surface of the sample, was used to induce the insulator-to-metal transition, and its fluence was controlled using a variable neutral-density filter (VF). The fluence of the probe beam was further attenuated to a value well below the insulator-to-metal threshold ($\phi_{probe} = 100\mu J/cm^2$), and we used its reflectivity from the sample to monitor the instantaneous optical properties of the VO_2 film. The probe pulses were directed along a variable delay stage to accurately control the relative timing between the pump and probe pulses by up to 4 ns with a few fs precision. The probe beam was focused on the sample at the same spot as the pump beam, using a shorter focal length lens. When tuned to the

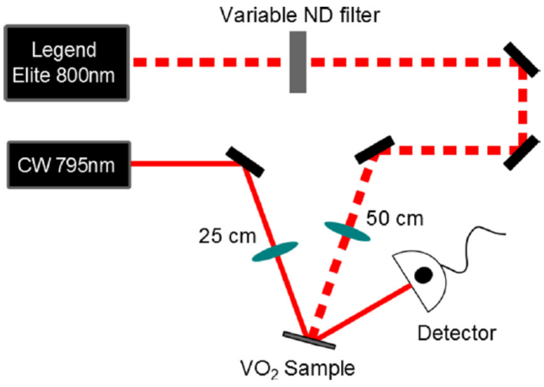

FIG. 7.2: Schematic of the experimental setup using a continuous-wave probe laser.

center of the pump beam focal spot, the smaller probe beam diameter (90 μm) ensured probing a region of uniform pump intensity. The reflected probe power was measured using a silicon photodetector, and further analyzed using a lock-in amplifier. To minimize the effects of probe pulse instabilities, as well as long-terms drifts due to environmental changes, we report the relative change in probe reflection R/R with the pump beam on or off. Notably, the MIT relaxation of the VO_2/TiO_2 sample was not measurable with the femtosecond probe, as its characteristic decay time exceeded the 4-ns maximum pulse separation, determined by the length of the delay stage. To measure the relaxation of the metallic VO_2 grown on the rutile sample, we modified our experimental setup by replacing the femtosecondprobepulseswithacontinuous-wave (CW)diode laser operating at 785 nm and a fast photodiode (measured response time of approximately 10 ns), as shown in Fig. 3. This detection method allowed us to measure changes in reflectivity for times longer than âĽĹ20 ns after the insulator-to-metal transition, that were inaccessible with the femtosecond probe arrangement.

Figure 7.1 shows sample measurements of both the VO_2/Al_2O_3 and VO_2/TiO_2 films, using the femtosecond and CW probe arrangements, respectively. The overall reflectivity depends on the refractive index of both the film and the substrate, and the refractive indices of TiO_2 and Al_2O_3 are different.Because it is easier to average the CW laser reflection signal, the curves for VO_2/TiO_2 are smoother than the curves for the VO_2/Al_2O_3.The rutile reflection spectra recorded using the ultrafast probe had the same noise as for the sapphire samples, indicating that the differences in the noise are due to differences in the probes, not in the samples.

For values of the pump fluence higher than a threshold, which depends on the substrate temperature,we can see that the reflectivity,soon after the pump pulse,remains almost constant for some time, i.e., its dynamics exhibits a “flat” region, see in particular Fig. 7.1(b). The observed “flattening” of the curves is due to the pump pulse heating the sample to a temperature above the threshold value for the thermally induced insulator-to-metal transition [20, 67]. In this case, the reflectivity stays unchanged at the level corresponding to a fully metallic phase until a non-negligible fraction of the sample cools down to the transition temperature. For all experimental curves, only the later exponential part of the measured reflectivity was included into the fitting thermal relaxation time analysis. The analysis of the relative reflectivity for both VO_2 samples demonstrates that after the initial rapid change during the ultrafast insulator-to-metal transition, its time evolution during the recovery is well fitted by a single exponential function with a recovery time constant τ:

$$R_{fit}(t) = R_I + (R_0 R_I) e^{t/\tau} \tag{7.1}$$

where R_I corresponds to the reflectivity in the insulating phase, and R0 corresponds to the reflectivity at t=0 s. The results of such measurements are shown in Fig. 4: for VO_2/Al_2O_3 films, we obtained values of τ of the order of few nanoseconds, whereas it took the VO_2/TiO_2 sample a few hundred nanoseconds to relax back to the insulating state. This two orders of magnitude difference in the recovery times was even more surprising considering that the characteristic times for the transition itself were quite similar, as

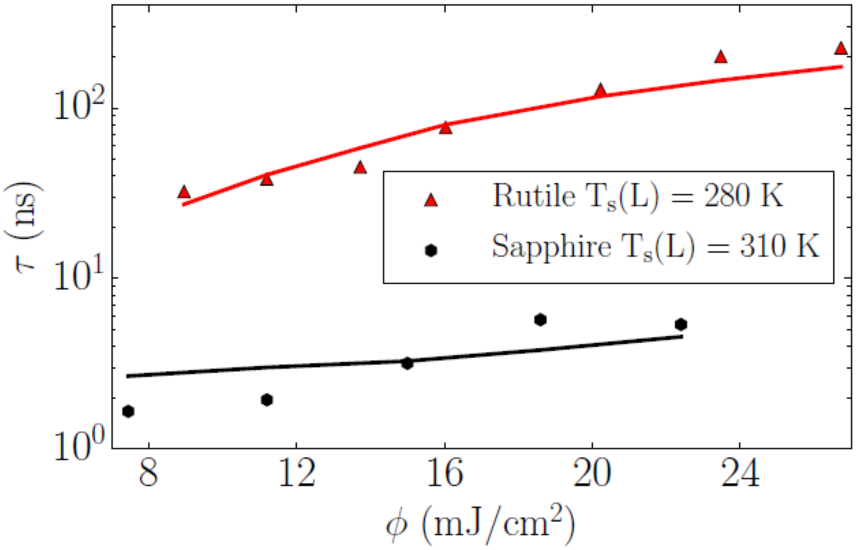

FIG. 7.3: Dependence of metal state decay constant τ on the laser pump fluence and substrate temperature. Dots represent experimental data and lines correspond to the results of the theoretical calculations.The initial temperature T_s for both sample substrates was approximately 30 K below their respective MIT critical temperatures.

demonstrated in previous studies [67]. In the discussion below, we demonstrate that the relaxation dynamics strongly depends on the microstructure of the VO_2 films, which in turn is strongly influenced by the properties of the substrate and their interface. Figure 7.3 also reveals that the rate of thermal relaxation for both samples increases with higher pump power.

7.1.1 THEORETICAL MODELING OF INHOMOGENEITIES

In order to take into account the effect of the inhomogeneities on the MIT dynamics, the first step is to characterize them.To do this,we can use the profile of the reflectivity across the thermally induced MIT. The dotted lines in Figs. 5(a) and 5(b) show the measured reflectivity as a function of temperature across the thermally induced MIT for a VO_2 film grown on sapphire and TiO_2, respectively. The temperature

Dependence of metal state decay constant τ on the laser pump fluence and substrate

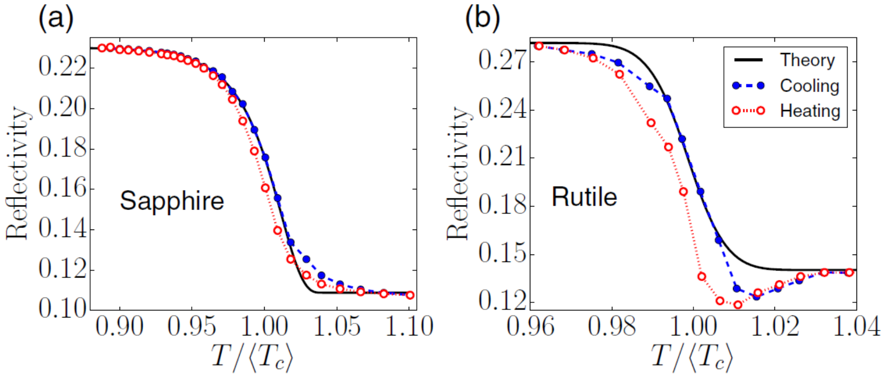

FIG. 7.4: Evolution of the reflectivity across the thermally induced MIT for the case of sapphire and rutile substrates normalized to the average critical transition temperature. The open circles (red) correspond to the measured reflectivity in the heating branch, the solid circles (blue) correspond to the measured reflectivity in the cooling branch, and the solid curve corresponds to the theoretical result. For rutile substrate $\langle T_c\rangle = 314\ K$, and for the sapphire substrate $\langle T_c\rangle = 340.1\ K$.

temperature. Dots represent experimental data and lines correspond to the results of the theoretical calculations.The initial temperature T_s for both sample substrates was approximately 30 K below their respective MIT critical temperatures.

driven MIT in VO_2 is a first-order transition. In the ideal case, the reflectivity is expected to exhibit a finite, step like change at the critical temperature Tc, at which the sample goes from a low-temperature insulating state to a high-temperature metallic state. In thin films, however, the optical reflectivity smoothly changes from the value corresponding to the insulating phase (R_I) to the value characteristic to the metallic phase (RM) as the temperature increases, as Fig. 5 illustrates. For our samples, the hysteresis loop is very narrow [45]. The fact that the MIT takes place over a range of temperatures implies that different regions of the sample have different values of Tc. This is different from the case of an ideal, homogeneous system for which the whole sample exhibits the coexistence of metallic and insulating regions only for T = Tc. As a consequence the MIT in the films is characterized not by a single critical temperature but by a distribution P(Tc) of critical temperatures. This is due to the fact that the VO_2 films are inhomogeneous:

they are formed by crystal grains with different local properties. Different grains in general have different sizes, slightly different stoichiometry, and experience different local strains. It is very challenging to characterize the distribution of all the local properties that can affect the transition temperature of each grain. However, for our purposes, we only need P(Tc) and, as we show below, this can obtained directly from the profiles of R(T) without having to characterize the distribution of the local properties affecting Tc. Let ÎůI be the fraction of the sample in the insulating phase. At a given temperature T , we have

$$\eta_I(T) = \int_T^{\infty} P(T_c)dT_c \tag{7.2}$$

Let Îům(T) = 1 âĹŠ ÎůI(T) be the fraction of the film in the metallic phase. To obtain the evolution of ÎůI(T) across the MIT, and therefore P(Tc), considering that changes in the fraction of the film that is metallic (insulating) are the dominant cause of changes in the reflectivity, we can use a two-fluid effective medium theory (EMT) [69, 70, 71, 72]. In the EMT, the inhomogeneous system is replaced by an effective homogeneous medium having the same,bulk,electric properties. Let be the dielectric constants (at the probing frequency)of VO_2 in the metallic and insulating phase, respectively. Then, the dielectric constant of the effective medium, EMT, is given by the following equation:

$$\frac{\eta_I(\epsilon_I - \epsilon_{EMT})}{\epsilon_{EMT} + g(\epsilon_I - \epsilon_{EMT})} + \frac{\eta_M(\epsilon_M - \epsilon_{EMT})}{\epsilon_{EMT} + g(\epsilon_M - \epsilon_{EMT})} = 0 \tag{7.3}$$

In Eq. 7.3, g is a factor that depends on the shape of the grain. Without loss of generality, we set g = 1/3. Let n and k be the real and imaginary parts, respectively, of the index of refraction, so that for the effective medium and therefore

$$R = \left| \frac{cos(\theta_0) - \sqrt{(n+ik)^2 - sin^2(\theta_0)}}{cos(\theta_0) + \sqrt{(n+ik)^2 - sin^2(\theta_0)}} \right|^2 \tag{7.4}$$

where corresponds to the probe incidence angle. Given our experimental setup, we can reliably obtain the imaginary part of the index of refraction by measuring the TABLEI. Comparative table between VO_2/TiO_2 and VO_2/Al_2O_3 sample parameters. VO_2/TiO_2 VO_2/Al_2O_3 T 314.0 K 340 1 K ÏČTc 2.6 K 8.8K 17.4 nm 64.7 nm] 13 nm 45 nm ÏČD 1.1 nm 38.5 nm nM +ikM RM 1.53 +i0.8 0.14 1.49 +i0.65 0.11 n_I $+ik_I$ R_I 3.03 + i0.57 0.28 2.60 +i0.60 0.23 σ_K 1100 $W/(Kcm^2)$ 13000 $W/(Kcm^2)$ absorption. For this reason, we set the value of the imaginary part of the complex index of refraction kM, (kI) for the metallic and (insulating) phase to the measured values, consistent with the values reported in the literature [3, 73],and then use Eq.7.4 and the measured value of R_M (R_I) in the metallic (insulating) phase to fix the corresponding value of n_M (n_I) (see Table I).

Using Eqs. 7.2 – 7.4, we can obtain the profile of R(T) across the MIT for a given $P(T_c)$. Assuming P(Tc) to be a Gaussian distribution, by fitting the measured profile of R(T) to the one obtained using Eqs. 7.2 – 7.4 we can obtain the average value of the critical temperature and its standard deviation σ_{T_c}. For VO_2/TiO_2 samples, we find 2.6 K, for VO_2/Al_2O_3 samples 8 K. The solid lines in Fig. 57.4 show the profiles of R(T) obtained using Eqs. 7.2 – 7.4 and the above values for $\langle T_c \rangle$ and σ_{T_c} .

The difference in the value of T_c between VO_2/TiO_2 and VO_2/Al_2O_3 samples can be attributed to the fact that TiO_2, having a rutile structure, might induce strains into the VO_2 film that should favor the metallic phase of VO_2. In general, strain effects are expected to play an important role in the physics of the MIT phase transition of VO_2 films. In our approach, such effects enter indirectly, via the form of the probability distribution $P(T_c)$, and the value of the thermal conductivity of the interface between the VO_2 film and the substrate.

As we discuss in the following section, for our theoretical treatment of the recovery dynamics over long time scales of VO_2 films the knowledge of $P(T_c)$, i.e., , is all that is needed. As mentioned before, the fact that σ_{T_c} is nonzero is due to inhomogeneities, of different nature, present in the VO_2 film. It is practically impossible to know the distribution in the films of the properties affecting T_c. However, it is interesting to consider the limit in which the grain size D is the dominant property affecting T_c. The reason is that in this limit it is possible to extract, using strong and fundamental arguments, the distribution P(D) for the grain size. In particular, it is possible to obtain the average grain size and its standard deviation, quantities that are of great practical interest. can be compared to estimates obtained using more direct experimental techniques, such as XRD. In the remainder of this section, we use the experimental results for R(T) across the MIT to extract and its standard deviation. Theoretical and experimental evidence [74] indicates that for thin films the distribution P(D) of the grain size D typically

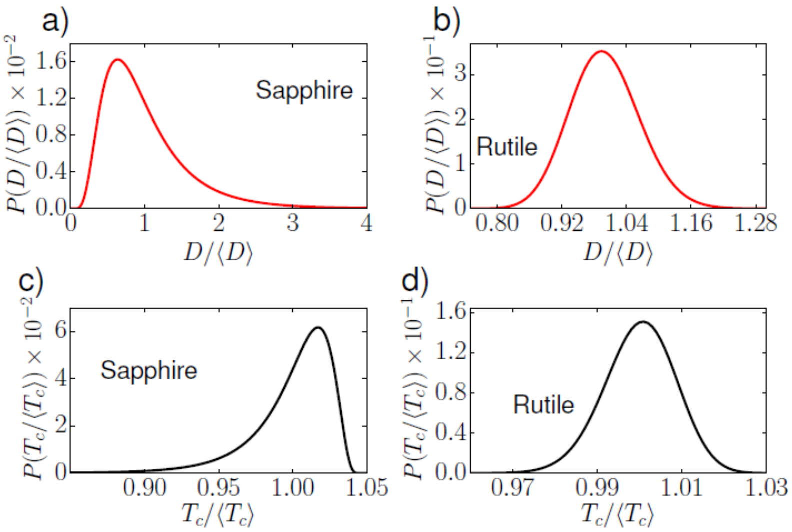

FIG. 7.5: (a) and (b) show the grain size distributions normalized to the average grain size for sapphire (64.7 nm) and rutile (4 nm) substrates, respectively. (c) and (d) show the critical temperature distribution normalized to the average critical temperature for sapphire (1 K) and rutile (0 K), respectively. The bulk critical temperature is taken to be T_c(bulk) = 355 K.

$$P(D) = \frac{1}{\sqrt{2\pi}\sigma D} exp[\frac{(lnD/\hat{D})^2}{2\sigma^2}] \tag{7.5}$$

In Eq. 7.5, D is the effective diameter of a grain, $\hat{D}$ is the grain size (diameter) such that $ln\hat{D} = \langle lnD \rangle$, and σ is the standard deviation of $ln(D)$.

From general and fundamental arguments [75, 76, 77, 78], we have

$$T_c = T_c^{(bulk)}(1 - \frac{1}{D/D_0}) \tag{7.6}$$

where T_c(bulk) is the bulk transition temperature and D_0, equal to 2 nm in our case, is the grain's diameter below which the grain is so small that is not possible to unambiguously identify its crystal structure. We set $T_c^{(bulk)} = 355\ K$, that is the temperature above which the VO_2/Al_2O_3 sample is completely metallic. This value is higher than the value of bulk VO_2 due to the strain experienced by the films [54, 24]. The relation between P(D) and P(T_c) is given by

$$P(T_c) = P(D(T_c))\frac{dD}{dT_c} \tag{7.7}$$

Using Eqs. 7.2 – 7.7, by fitting the measured profile of R(T) across the MIT, we can obtain P(D) and therefore and its standard deviation. Figures 6(a) and 6(b) show the profiles of P(D) used to obtain the good theoretical fit to the evolution of R(T) shown in Fig. 5. These profiles correspond to 7 nm and ÏČD = 38.5 nm for the VO_2/Al_2O_3 samples,and 4 nm and ÏČD = 1.1 nm for the VO_2/TiO_2 samples. It is interesting to compare the values of obtained using this approach to the values estimated using XRD. From XRD data [67], we estimated 45 nm for VO_2/Al_2O_3 and 13 nm for VO_2/TiO_2 (see Table I). These values are in remarkable semiquantitative agreement with the values extracted from the profiles of R(T) across

FIG. 7. Evolution of the insulating partial volume ÎůI across the thermally induced MIT for case of (a) sapphire and (b) rutile substrates. For rutile, 0 K and for sapphire 1 K.

the MIT suggesting that the assumption that the grain size is the dominant property affecting the local value of T$_c$ might be qualitatively correct. It is therefore interesting to obtain the profiles of P(T$_c$) corresponding to the distributions of grain sizes shown in Figs. 6(a) and 6(b). Such profiles are shown in Figs. 6(c) and 6(d). The evolution of ÎůI(T) across the MIT obtained using these profiles is shown in Fig. 7. Our analysis suggest that the R(T) profiles could be an indirect method to characterize the distribution of grain sizes in VO$_2$ films, a very challenging quantity to obtain using direct imaging experiments.

7.2 THEORETICAL MODELING OF THE RELAXATION DYNAMICS OF THE MIT

In our experiment, the VO$_2$ films have a thickness d equal to or smaller than 110 nm (see Fig. 7.6), which is comparable with the laser 1/e penetration depth 110âĂŞ130 nm [67]. Thus we can assume that the pump pulse heats the film uniformly throughout its thickness. To describe the heat transfer process between the film and the substrate, we assume the temperature

to be uniform throughout the film for all times. Effectively, given these conditions, the heat transfer problem becomes a one-dimensional problem, and the equation for the rate of change of the heat (Q) in the film takes the form (8) where T$_f$ is the film temperature, A is the area of the film, ÏĄI (ÏĄM) is the density in the insulating (metallic) phase, ÏĄav âĽą (ÏĄI + ÏĄM)/2, CI (CM) is the heat capacity in the insulating (metallic) phase, L is the specific heat, and P(Tf)dTf is the fraction of the sample undergoing the MIT in the time interval dt during which the film temperature is in the interval [Tf ,Tf + dTf]. Here, P(Tf) is the distribution of critical temperatures due to the inhomogeneities that we have obtained in the previous section. Using Eq.7.2 and the fact that ÎůM = (1 âĹŠ ÎůI), we can rewrite Eq. (8) in a form that more explicitly shows the effect due to

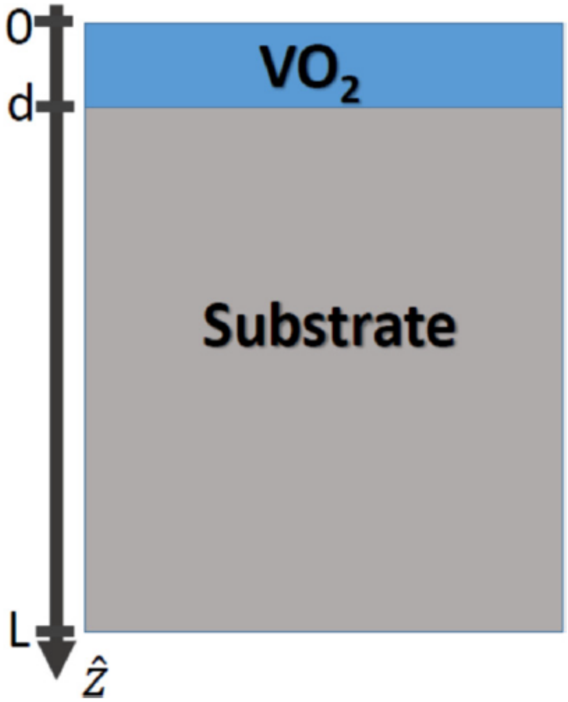

FIG. 7.6: Sketch of the heterostructure considered in this work. It is composed of a vanadium dioxide (VO_2) thin film deposited on top of a substrate. The substrates considered in this work are titanium dioxide (TiO_2), and aluminum oxide (Al_2O_3). For VO_2/TiO_2, d = 110 nm while for VO_2/Al_2O_3, d = 80 nm. For both substrates, L = 0.5 mm.

the inhomogeneities, i.e., the fact that the MIT is not characterized by a single T_c, but by a distribution of T_câĂŹs: (9) Equation(9)isthemainresultofourwork:itallowstoproperly take into account the effect of inhomogeneities on the long time-scale dynamics across a first-order phase transition. The key quantity entering Eq. (9) is the distribution $P(T_c)$ that, as we have shown in the preceding section, can be obtained from the profile of R(T) across the thermally activated MIT. Our work is the first to combine the information from the thermally activated MIT to obtain a physically accurate heat equation to describe the recovery dynamics after a photoinduced MIT. For the latent heat, we have [75, 76, 77] , (10) where L(bulk) is the value of the specific heat for bulk VO_2. Given Eq. (6), Eq. (10) implies L = L(bulk)(1 âĹŠ D0/D). The rate of change of heat in the film given by Eq. (8) must be equal to the heat current (JQ) across the interface between the film and the substrate: JQ = âĹŠÏČKA(Tf âĹŠ Ts(d)), (11) where ÏČK is the Kapitza constant characterizing the thermal conductivity of the interfaces [79, 80, 81, 82], and Ts(d) is the temperature of the substrate at the surface facing the VO_2 film. Combining Eqs. (9) and (11), for Tf , we obtain the equation

In Eq. (12), the only undetermined quantity is ÏČK. We fix ÏČK by fitting the theoretically obtained time evolution of R(t) to the one measured experimentally, for fixed experimental conditions such as the temperature of the substrate and the pump fluence. The robustness of the theory presented is evidenced by the fact that, the same fixed value of ÏČK provides agoodagreementbetweenthetheoreticalandtheexperimental results for a broad range of experimental conditions. To completely define the problem, we need to supplement Eq. (12) with proper boundary conditions. The temperature distribution within the substrate, Ts(z,t), satisfies the diffusion equation: , (13) where ks, Cs, ÏĄs are the thermal conductivity, heat capacity, and mass density, respectively, of the substrate. The bottom of the substrate, for which z = L (see Fig. 7.6, is kept at a fixed temperature . At the film/substrate interface, the heat transferred from the film must be equal to the heat current ksâĹĆTs/âĹĆz|z=d. We then have that the boundary conditions completing Eq. (13) are ; (14) = âĹŠÏČ T (t) âĹŠ Ts(z = d,t)). (15) Equations ( ), combined with knowledge of the distribution P(T_c) completely define the temperature evolution of the VO_2 film. Notice that in these equations the only unknown parameter is the Kapitza constant ÏČK. All the other quantities are known from direct measurements. P(T_c) is obtained from the profile of R(T) across the MIT, independently from the dynamics of R after the photoinduced insulator-to-metal transition. Also, the relation between the specific heat L and T is fixed by general and fundamental results [75, 76, 77]. While these equations can in general be solved only numerically, some qualitative understanding of the decay time τ can be gained if we make some simplifications. Let (c)]. At a temperature T , the insulating volume fraction is given by

FIG. 9. Full numerical calculation of the dependence of metal state decay constant τ on σ_{T_c} for two different values of the sample average critical temperature 280 K.

The initial temperature T0 = 360 K is such that the sample is initially fully metallic, and (

FIG. 10. VO_2/Al_2O_3 metal state decay time τ dependence on the Kapitza constant 7 nm, ÏČD = 38.5 nm, substrate temperature Ts(L) = 310 K, and fluence ÏĘ = 8mJ/cm^2. The red dots correspond to numerical calculations, and the dashed line is given by τ âĹİ ÏČKâĹŠ1.

Then assuming that the pump pulse is strong enough to drive the entire film into a fully metallic state at t = 0, the time dependence of the insulating volume fraction can be approximated by a simple exponential form ÎůI(t) = 1 âĹŠ AeâĹŠt/τ. In this case, an expression for the temperature can be obtained through the relationship ÎůI(T (t)) = ÎůI(t). Furthermore, assuming that the substrate temperature Ts does not change with time, and the latent heat L to be temperature-independent, we can calculate the decay constant τ:

$$\tau = Cd\frac{\sigma_{T_c}}{\sigma_K}\frac{C_M\rho_M + L\rho_{av}P(T_0))}{T_0 - T_s} + \tau_0 \tag{7.8}$$

where the constants C $>$ 0, and τ_0 can only be determined by solving the full system of equations (12)–(15). It is interesting to note that despite its many limitations, Eq.**??**(16)capturesmanyimportantqualitativetraitsoftheactual relaxation process. For example, Fig. 9 shows a plot of the decay constant as a function of σ_{T_c} obtained solving the full system of equations (12)âĂŞ(14) for two different values of the averagecriticaltemperature,andsameinitialtemperatureT0 $=$ 360 K. It is easy to see that the decay time τ follows the linear trend predicted by Eq.**??** (16) in the limit (. Similarly, an exact solution shows the inverse dependence of τ on the Kapitza constant, τ âĹİ ÏČKâĹŠ1, as shown in Fig. 10. The relation (16) is another important result of our work, it shows how the characteristic time of the recovery dynamics is related to the properties of the VO_2 films. In particular, it shows the novel result that τ grows linearly with σ_{T_c}, the standard deviation of P(T$_c$). σ_{T_c} can be reliably obtained from the profile of R(T) across the MIT.

7.3 EFFECT OF INHOMOGENEITIES ON THE RELAXATION DYNAMICS OF THE PHOTOINDUCED MIT

Using the theoretical approach described in Sec. IV, we can obtain the time evolution of the optical reflectivity R through the MIT, as well as explain the significant difference in relaxation time scales between the two VO_2 samples TABLE II. Parameters of VO_2 and substrates. VO_2 heat capacity insulating phase CI [60] 0.656 J/(g K) heat capacity metallic phase CM [60] 0.78 J/(g K) density insulating phase ÏĄI [82] 4.57 g/cm^3 density metallic phase ÏĄM [82] 4.65 g/cm^3 thermal conductivity insulating phase ÎžI [83] 3.5 W/(m K) thermal conductivity metallic phase ÎžM [83] 6 W/(m K) bulk latent heat L(bulk) [60] 51.8 J/g TiO_2 heat capacity Cs [84] 0.686 J/(g K) density ÏĄs [82] 4.25 g/cm^3 thermal conductivity Îžs [85] 8 W/(m K) Al_2O_3 heat capacity Cs [86] 0.779 J/(g K) density ÏĄs [86] 3.98 g/cm^3 thermal conductivity Îžs [86] 30 W/(m K) VO_2/TiO_2 absorption coefficient at 800 nm α [67] 0.01 nm^1 VO_2/Al_2O_3 absorption coefficient at 800 nm α [67] 0.0076 nm^1 considered. In all the numerical calculations, we assume CI, ÏĄI, CM, and ÏĄM to be equal to the bulk values for insulating and metallic VO_2, see Table II. The initial film temperature is fixed by the pump fluence taking into account the Gaussian profile of the pulse and the fact that some of the heat is lost by the film during the time interval [0,t0] for which our analysis does not apply, t = 0 is time at which the pump pulse hits the VO_2 film and t0 = 10 ns for VO_2/TiO_2 films and t0 = 0.5 ns for VO_2/Al_2O_3 films.

FIG. 12. Dependence of the VO_2/TiO_2 metal state decay time constant τ on ÏČD for two values of , as defined in Eq. (5), Kapitza constant ÏČK = 1100W/(Kcm^2), substrate temperature Ts(L) = 280 K, and initial fluence ϕÏĘ = 9 mJ/cm^2.

As discussed in Sec. IV, ÏČK is the only unknown parameter. For the case of VO_2/TiO_2 samples, by fitting one of the curves for the dynamics of the reflectivity, we find ÏČK = 1100W/(Kcm^2). We find that all experimental curves are well approximated assuming the same value for the Kapitza constant, see Fig. 7.7(a). For the case of VO_2/Al_2O_3, the characteristic time scale of the recovery is much shorter than for VO_2/TiO_2 samples. As discussed in Sec. III, the two sampleshaveverydifferentinhomogeneities:σ_{T_c} isalmostfour times larger in VO_2/Al_2O_3 than VO_2/TiO_2. All other things being equal, Eq. (16) implies, see Fig. 12, that τ should be largerinVO_2/Al_2O_3 thaninVO_2/TiO_2,theoppositeofwhatis observedexperimentally.WearethenledtoconcludethatÏČK in VO_2/Al_2O_3 mustbemuchhigherthaninVO_2/T shows the measured evolution of R for the VO_2/Al_2O_3 sample for a fixed value of the fluence ÏĘ and substrate temperature, and the theoretical curves for this case that we obtain

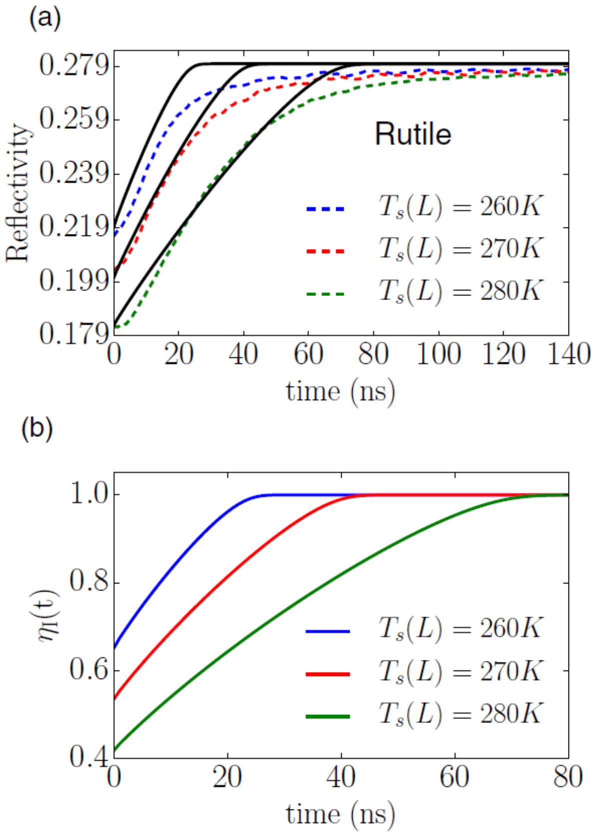

FIG. 7.7: (a) Time evolution of reflectivity after the photoinduced MIT for VO_2/TiO_2 for three different T_s(L) and ϕÏĘ = 9 mJ/cm^2. The solid curves correspond to the theoretical results, and the dashed curves correspond to the experimental results. For the three theory curves, we use ÏČK = 1100W/(Kcm^2). (b) shows the corresponding insulating fraction time evolution.

using the distribution P(T_c) obtained for VO_2/Al_2O_3 and two different values of ÏČK. We see that by choosing for ÏČK the same value used for VO_2/TiO_2, there is no agreement between FIG. 14. Film and substrate temperature time evolution. For sapphire (a), Ts(L)

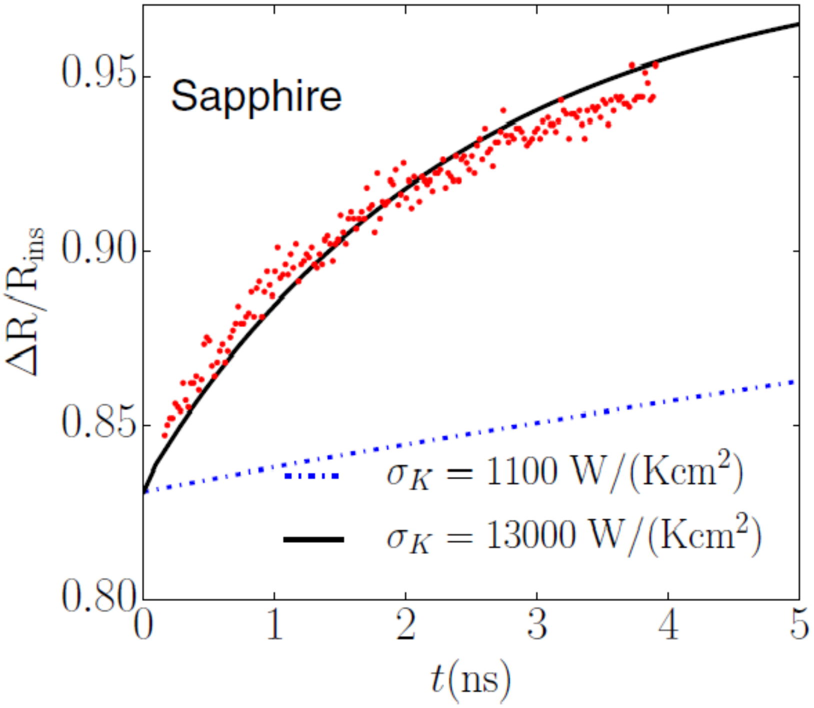

FIG. 7.8: VO_2/Al_2O_3 reflectivity time evolution after photoinduced MIT for ϕ = 7.5 mJ/cm^2.The red dots correspond to the experimental result. The dotted curve correspond to the theory with σ_K = 1100 W/(Kcm^2), and the solid curve corresponds to σ_K= 13000 W/(Kcm^2).

= 310 K, and for rutile (b), Ts(L) = 280 K.

theory and experiment. By setting ÏČK = 13000W/(Kcm^2), we obtain excellent agreement. Indeed, all the experimental curves R(t) for VO_2/Al_2O_3 are well approximated by the theoretical results assuming ÏČK = 13000W/(Kcm^2). Figure 14 shows the time evolution of the VO_2 film and substrate temperatures (close to the interface) for the VO_2/Al_2O_3 film, panel (a), and for the VO_2/TiO_2 film, panel (b), using the parameter values summarized in Table II. It helps to qualitatively understand the differences in the thermal relaxation between the two samples. Due to the lower values of the Kapitza constant, thermal energy stays more concentrated near the VO_2-TiO_2 interface, keeping the temperature of the VO_2 film above T_c longer. To investigate the temperature dependence of the thermal relaxation, we repeated the measurements while changing the base substrate temperature of the VO_2/TiO_2 sample. For these measurements, the sample was placed inside a cryostat, and cooled down to temperatures T_s(L) between 260 K and 298 K. The results of these measurements, along with the theoretical calculations,are shown in Fig.15.We again observe a good semiquantitative agreement between theoretical and experimental results. Also, note that the simple expression for the decay constant τ, Eq. (16), captures the overall decay rate drop at lower substrate temperatures T_s(L). We point out that all the theoretical curves are obtained using the fixed set of parameters shown in Table II. As mentioned above, the only unknown parameter that enters the theory is σ_K. In the results presented above, σ_K was fixed

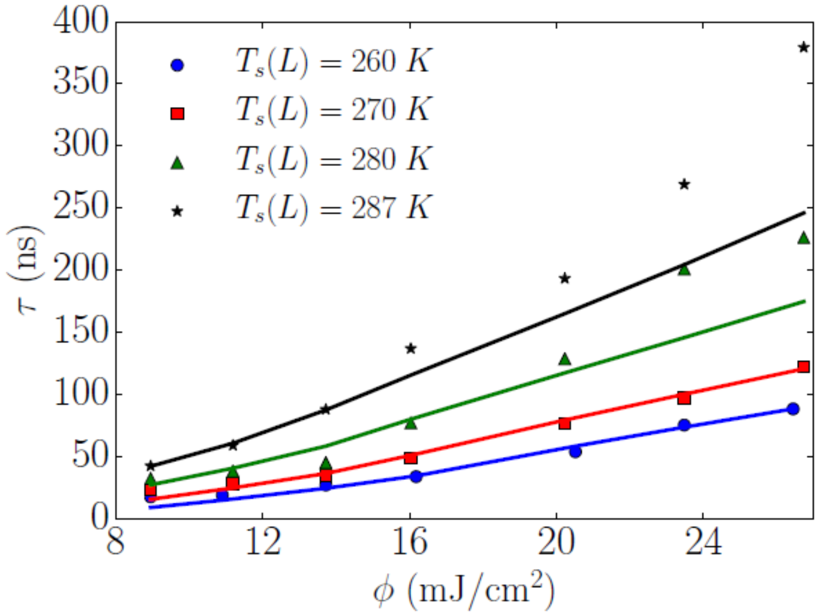

FIG. 7.9: Dependence of metal state decay constant τ on fluence and substrate temperature for VO_2/TiO_2.

to a single value for each film, and this value was then used to obtain the results for a range of experimental conditions with different substrate temperatures and pump fluences. For example, Fig. 4 shows an excellent agreement between the experimental measurements and theoretical calculations across the entire range of pump fluences, limited on the lower end by our ability to reliably detect the variation in the probe reflectivity, and on the upper end by the damage threshold of our sample (pump fluence $>$40mJ/cm^2). VI. CONCLUSIONS In conclusion, we have presented a combined experimental and theoretical study of the long time-scale recovery dynamics of VO_2 films following an ultrafast photoinduced insulator-tometal transition. We have developed a theoretical approach that is able to properly take into account the effect of inhomogeneities. The main results of our work are (i) the derivation of the generalized heat equation (9) that properly takes into account that during the recovery, due to the inhomogeneities, only fraction of the sample is undergoing the metal-to-insulator transition and correctly tracks the evolution in time of the metallic (insulating) phase; (ii) the clarification of the connection between the temperature-dependent profile (R(T)) of the reflectivity across the thermally induced MIT and its dynamics after a photoinduced insulator-to-metal transition; (iii) the approximate relation, Eq. (16), between the characteristic time of the recovery dynamics and the parameters of the film, in particular to the standard deviation of the distribution of critical temperatures as extracted from R(T); and (iv) the ability of our theory to describe, using a fixed value of the Kapitza constant, the recovery dynamics for different values of the substratetemperature and pump fluence. By changing the pump fluence the characteristic time of the recovery can be changed, experimentally, by two orders of magnitude: our theory is able to account for such a change. The theoretical approach that we present is general and can be used to describe the dynamics (in the adiabatic limit) of inhomogeneous systems across a first order phase transition. The approximate relation between the characteristic time τ and the parameters of the system shows that τ is directly proportional to the width of the thermally activated transition. This result allows to estimate the recovery time of VO_2 films solely on the basis of a measurement of R(T) across the MIT. Assuming that variations of the size of the grains forming the films are the main source of inhomogeneities, using very general and fundamental relations between the grain size and the grainâĂŹs critical temperature, we have been able to obtain the distribution of the grain sizes. In particular, we have been able to estimate the average grainâĂŹs size and its standard deviation. WefindthatthecalculatedaveragegrainâĂŹssizeisinremarkable semi-quantitative agreement with the one obtained from XRD measurements. For systems in which inhomogeneities are mostlyduetovariationsofthesizeD ofthegrains,ouranalysis provides a way to obtain the size distribution P(D) from the temperature dependent profile of the reflectivity across the thermally induced MIT. This could be very useful considering that P(D) is a very challenging quantity to obtain via direct measurements.

CHAPTER 8

Pumping VO_2 films with THz pulses

Of all the correlated materials that undergo semiconductor-to-metal transitions, vanadium dioxide (VO_2) has been one of the more intensively studied. Its close-to-room transition temperature (at about 340 K in bulk) makes it a convenient study material for both fundamental studies and also for a wide range of potential applications. The mechanism behind the transition is also still hotly debated, despite several decades of study [14, 35, 19, 87, 46]. In the semiconductor-to-metal transition there are two processes observed. The lattice structure changes from lower symmetry monoclinic structure to a higher symmetric tetragonal structure (Peirls transition). There is also a collapse of the $d_{\asymp}$ bands, consistent with a Mott transition. To probe the ultrafast dynamics of MIT transition, induced by a sub-ps electromagnetic pulses, a typical pump-probe configuration is used, in which a strong pulse is used to enable the transition, and a weaker pulse, arriving after a controllable delay, reveals changes induced in the electrical and/or optical properties of a VO_2 thin film as a function of time after the original pump pulse. Looking at the femtosecond scale has allowed researchers to separate the two mechanisms by looking at the scale at which the phase transition happens, since the thermal response happens on a longer time scale. [35] The most traditional pump-probe arrangement for studing VO_2 relies on an optical pump, and either an optical or THz probe. Many experiments use optical pulses at an 800 nm central wavelength, since these can be produced by a Ti:Sapph femtosecond lasers; also, the photon energy is sufficient to bridge the VO_2 band gap of ~ 0.7 eV.[1]. Very recently, however, a few experiments reported observation of the VO_2 phase transition induced by strong THz pulses [? ? ?]. Unlike an optical pump, such pulses are not sufficient to photoexcite the film. Thus, they offer a new perspective on studies of the MIT transition mechanism, as well as open new possibilities for applications.

Here we report on experiments using low-power ($<$ 100 kV/cm) broadband pump pulses in the 0-12 THz spectral range to induce a partial insulator-to-metal transition in a VO_2 thin film, manifested by a change in the optical transmission. Our results demonstrate the possibility of inducing the transition at a significantly lower THz power, compared to previous results [? ?], and thus provide an interesting new avenue for low-energy THz control of the VO_2 insulator-metal phase transition. In addition, unlike previous studies, we observe a slower dynamics in the THz-induced transition compared to the photo-induced one. We also investigate the potential role of a resonance interaction with IR-active phonon modes for VO_2, revealing the crucial role of the higher-frequency component of the THz pump pulse used.

For these measurements we used a 110 nm-thick VO_2 film grown on 500μm (011) TiO_2 substrate; detailed characterization of this film is reported in [45]. The film is epitaxial and mono-crystalline, and an out of plane orientation of (011). The critical temperature for the thermally-induced MIT was found to be $T_c = 310$ K, with a hysteresis loop width of 9 K, as we would expect for a crystalline film with strain from the mismatch of the substrate and lattice [65, 23, 88, 52].

We measured the film in a pump-probe configuration, with a THz pump with a frequency range of 0-12 THz and a probe at 800 nm. The THz pulse was produced with

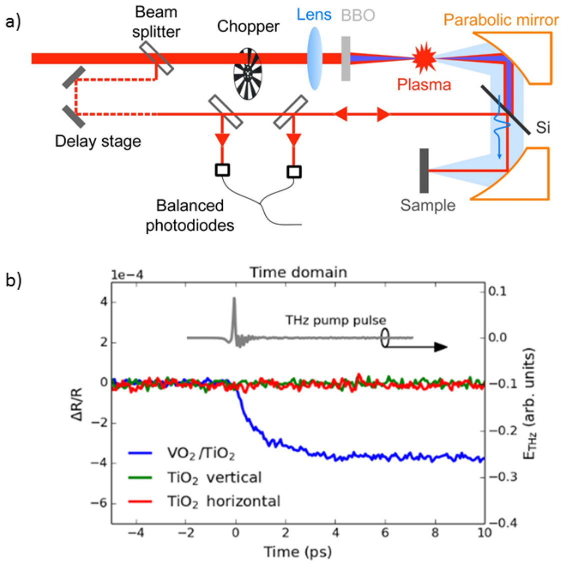

FIG. 8.1: (a) Schematics of the THz pump - optical probe experimental setup. (b) Optical probe reflection by the VO_2 film on a TiO_2 substrate and by the TiO_2 substrate only after interaction with the THz pump pulse.

a shaped 800 nm, 35 fs pulse.The beam was split and one leg was frequency doubled with a BBO. Both pulses were then focused in a contained volume purged with nitrogen, producing the THz pulse. The THz pulse has 10% of the peak field above 100 kV/cm.

Another 800 nm pulse was sent to a delay stage before being reflected off the front of the sample, so that the reflection could be probed in the optical range, as can be seen in figure 8.1 b). The absorption of the THz pump by the sample was measured with a silicon wafer. The THz pump changes the optical properties of the Si wafer in the near-IR and the intensity of this response can be measured with the 800 nm probe pulse. The probe was measured in both cases with a balanced detector to reduce noise.

Using such pump-probe arrangement we have observed a small, but clearly detectable change in the optical probe reflection of VO_2 after the interaction with the THz pump pulse. An example of the recorded signal is shown in Fig. 8.1(b). We see that immediately after the THz pump pulse arrival, the reflectivity of the VO_2 film starts to drop.Because of the low energy of the THz pulses, the observed relative change is significantly smaller than the value corresponding to the complete transition to a fully metallic VO_2 film [**?**]; nevertheless, the reflectivity drop is detectable with excellent signal-to-noise discrimination. Moreover, to verify that the observed reflectivity variation is due to the VO_2 film only, and not due to substrate itself, we repeated the measurements using a clean TiO_2 substrate, and clearly observed the absences of any changes in the probe reflection before and after the pump pulse.

We then investigated the dependence of the optical response as a function of the THz pump pulse energy, and observed the expected reduction of the reflectivity change $|\Delta R|/R$ for weaker pump pulses, as can be seen in Fig. 8(a). Interestingly, the dynamical change in reflectivity does not depend on the pump energy (at least in the experimentally tested range). To illustrate that, Fig. 8(b) displays the normalized reflectivity curves; it is easy to see that they overlap exactly (within the experimental noise).

It is important to compare the THz-induced MIT with that induced by an IR optical pulse. The black curve in Fig. 8(b) represents the typical behavior of the optical reflectivity after a partial MIT induced by an approximately 100 fs optical pulse at 800nm wavelength on the same film,and a comprehensive analysis of the VO_2 photo-induced MIT dynamics in such case can be found in Refs. [20, 67]. In both cases we observed an instantaneous response after the arrival of the pump pulse. However, the dynamics of the transition observed in our experiment now differs: while the IR optical pump pulse induced almost a step-like change at a timescale comparable with the pump pulse duration, the optical response triggered by a THz pump pulse of similar duration took a few ps to reach its new quasi steady state level that persists for several nanoseconds. This change can be fitted with an exponential with a time constant of $\tau = 0.90 \pm 0.02$ ps. The differences in the transition dynamics arise from the difference in transition mechanism induced by the two different pump pulses. The optical photons have energy higher than the VO_2 bandgap,

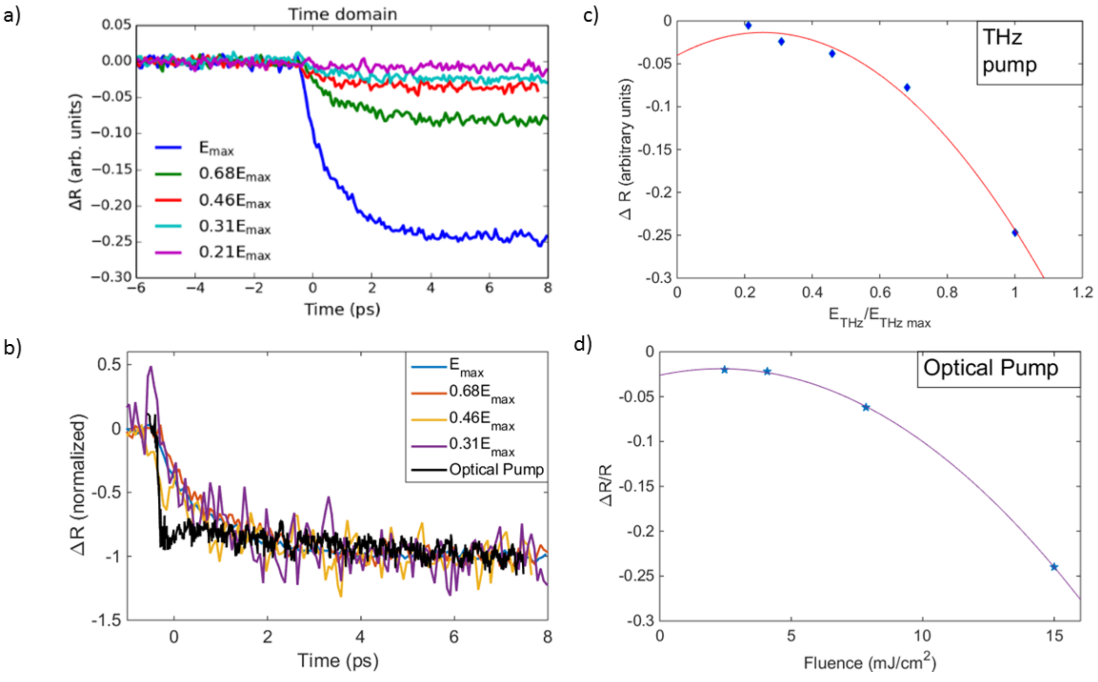

FIG. 8.2: a) shows the probe reflectivity response as the THz pump is attenuated. b) shows all the curves, normalized with respect to the max pump power of 100 kV/cm. Note that they all have the same rate of change over time before the change in reflection flattens out. This is different than the behavior of the film when pumped optically. c) and d) show the relationship between pump power and the resulting change in reflection for THz and 800 nm respectively.

and their absorption produce a photo-excited electron population, that can be a driving force in the insulator-to-metal transition that follows. However, a significantly lower THz photon energy does not allow such mechanism.

Recent publications reporting THz-pulse induced transitions in VO_2 film also reported step-like variation of the film response when using significantly higher pump pulse energies. In this regime the observed changes in the VO_2 film properties can be explained by the THz radiation-induced tunneling of electrons [?]. However, this mechanism is expected to play a leading role for strong THz electric fields, exceeding the values used in our experiment. On the other hand, the THz radiation can interact directly with the VO_2 lattice, resulting in slower changes. In particular, direct measurements of the structural dynamics reported by [89] for an epitaxially strained thin $VO-2$ film reveal changes in the lattice happening at the time scale of a few ps, comparable with the optical response observed in our experiments.

We attempt to better understand the role of the frequency composition of the THz pump pulse. Previous studies identified the critical lattice vibration modes responsible for the structural transition to be Raman-active modes. In particular, the 6 THz Ag mode of the monoclinic (insulating) VO_2 crystal that maps onto the rutile (metallic) VO_2 crystal is believed to be the important mode in inducing the structural phase transition in the lattice. Clearly, one cannot directly access any Raman-active modes using a direct THz excitation; however, there exist mechanisms for coupling between IR-active and Raman active modes [90]. Moreover, transient oscillations at 5.9 THz were observed in optical response of a VO_2 film after excitation by an intense multi-terahertz excitation. For example, this may imply that one of the IR-active modes is coupling with the 6 THz Ag mode, allowing us to observe the lattice response.

These facts suggest that THz radiation at frequencies around 6 THz may have the strongest effect on the MIT in this film. Since direct analysis of the VO_2 absorption spectra in our experiment was made impossible by the broadband absorption of the THz radiation by the substrate material (TiO_2), we relied on a spectral filtering technique to determine the relative contributions of the different THz frequencies. In particular, we compare the optical response of the VO_2 when using a full-bandwidth pump pulse (approximately $0-12$ THz) and when the frequency components above approx. 3 THz were blocked before interacting with the sample. Fig. 8(a,b) shows the temporal and spectral profiles of the two pump pulses, used in this measurement. We also made sure that that the peak electric fields for both pulses were the same. Fig. 8(c) clearly shows that while the attenuated broadband THz pulse produced a clear change in the film's reflectivity, the filtered pulse fails to do so. This implies the critical role of the higher-frequency components in the THz-induced MIT, at least for the regime of weak THz pump pulses.

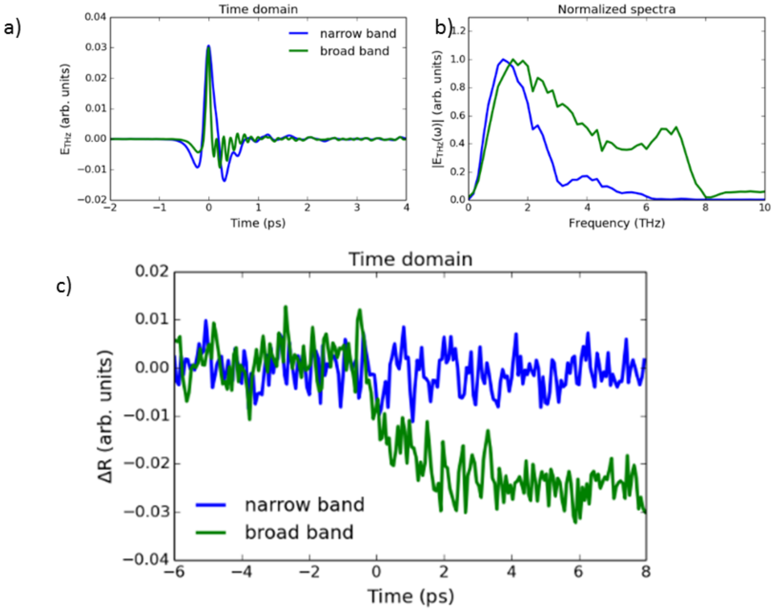

FIG. 8.3: Electric field temporal profiles (a) and spectra (b) for an attenuated broadband and spectrally filtered THz pump pulses. (c) Recorded optical response of the VO_2 film to these THz pump pulses.

In conclusion, we report the observation of the metal-to-insulator transition in a monocrystalline 110-nm VO_2 film, induced by a low-energy THz pulses. Using a THz pump - IR probe experimental arrangement, we demonstrate that the THz pump pulse produces a long-lasting effect on the optical response of the film that we can attribute to the onset of a partially metallic state. We observed a clear nonlinear dependence of the observed variation with THz pulse energy, with a threshold value around 20 kV/cm. The change in optical reflectivity did not happen instantaneously, like in the case of the optical pump pulses or previously reported experiments with strong THz pulses; instead it followed an exponential decay with a time constant around 1 ps. This slower response hints that the transition may be triggered by the resonant interaction of the THz pump with the VO_2 lattice. This suggestion is supported by the fact that when the frequency components above 3 THz are removed from the pump pulse, the optical response disappears, compare to the broad-band pulse with the same peak electric field.

CHAPTER 9

Conclusion and Outlook

BIBLIOGRAPHY

[1] J. B. Goodenough, Journal of Solid State Chemistry **3**, 490 (1971), ISSN 00224596, URL `http://dx.doi.org/10.1016/0022-4596(71)90091-0`.

[2] M. Imada, A. Fujimori, and Y. Tokura, Reviews of Modern Physics **70**, 1039 (1998), ISSN 0034-6861, URL `http://rmp.aps.org/abstract/RMP/v70/i4/p1039_1` `http://link.aps.org/doi/10.1103/RevModPhys.70.1039`.

[3] H. Verleur, A. B. Jr, and C. Berglund, Physical Review (1968), URL `http://prola.aps.org/abstract/PR/v172/i3/p788_1`.

[4] R. W. G. Wyckoff, *Crystal Structures*, vol. 1 (Interscience Publishers, New York, New York, 1963), 2nd ed.

[5] A. Zylbersztejn and N. Mott, Physical Review B **11**, 4383 (1975), URL `http://journals.aps.org/prb/abstract/10.1103/PhysRevB.11.4383` `http://prb.aps.org/abstract/PRB/v11/i11/p4383_1`.

[6] F. F. Morin, Physical Review Letters **3**, 2 (1959), ISSN 0031-9007, URL `http://link.aps.org/doi/10.1103/PhysRevLett.3.34` `https://noppa.tkk.fi/noppa/kurssi/ke-35.2100/luennot/KE-35_2100_mit-efekti.pdf`.

[7] D. N. Basov, R. D. Averitt, D. van der Marel, M. Dressel, and K. Haule, Reviews of Modern Physics **83**, 471 (2011), ISSN 0034-6861, URL `http://link.aps.org/doi/10.1103/RevModPhys.83.471`.

[8] R. Pynn, J. Axe, and P. Raccah, Physical Review B **17**, 2196 (1978), ISSN 0163-1829, URL `http://link.aps.org/doi/10.1103/PhysRevB.17.2196`.

[9] E. Abreu, M. Liu, J. Lu, K. G. West, S. Kittiwatanakul, W. Yin, S. A. Wolf, and R. D. Averitt, New Journal of Physics **14**, 083026 (2012), ISSN 1367-2630, URL `http://stacks.iop.org/1367-2630/14/i=8/a=083026?key=crossref.667002eceb37a540885b`

[10] J. Lu, K. G. West, and S. a. Wolf, Applied Physics Letters **93**, 262107 (2008), ISSN 00036951, URL `http://link.aip.org/link/APPLAB/v93/i26/p262107/s1&Agg=doi`.

[11] S. Kittiwatanakul, J. Lu, and S. a. Wolf, Applied Physics Express **4**, 091104 (2011), ISSN 1882-0778, URL `http://stacks.iop.org/1882-0786/4/091104` `http://apex.jsap.jp/link?APEX/4/091104/`.

[12] T. Kikuzuki and M. Lippmaa, Applied Physics Letters **96**, 132107 (2010), ISSN 00036951, URL `http://link.aip.org/link/APPLAB/v96/i13/p132107/s1&Agg=doi`.

[13] N. Aetukuri, A. Gray, M. Drouard, and M. Cossale, Nature Physics pp. 1–17 (2013), URL `http://www.nature.com/nphys/journal/v9/n10/abs/nphys2733.html`.

[14] A. Zylbersztejn and N. Mott, Physical Review B (1975), URL `http://journals.aps.org/prb/abstract/10.1103/PhysRevB.11.4383`.

[15] N. V. Smith, Physical Review B **64**, 1 (2001), ISSN 0163-1829.

[16] W. R. Roach and I. Balberg, Solid State Communications **9**, 551 (1971), ISSN 00381098.

[17] M. Becker and A. Buckman, Applied physics . . . **65**, 1507 (1994), URL `http://ieeexplore.ieee.org/xpls/abs_all.jsp?arnumber=4883887` `http://scitation.aip.org/content/aip/journal/apl/65/12/10.1063/1.112974`.

[18] A. Cavalleri, T. Dekorsy, H. Chong, J. Kieffer, and R. Schoenlein, Physical Review B **70**, 161102 (2004), ISSN 1098-0121, URL `http://link.aps.org/doi/10.1103/PhysRevB.70.161102`.

[19] D. J. Hilton, R. P. Prasankumar, S. Fourmaux, A. Cavalleri, D. Brassard, M. A. El Khakani, J. C. Kieffer, A. J. Taylor, and R. D. Averitt, Physical Review Letters **99**, 1 (2007), ISSN 0031-9007, URL `http://link.aps.org/doi/10.1103/PhysRevLett.99.226401`.

[20] T. Cocker, L. Titova, S. Fourmaux, G. Holloway, H.-C. Bandulet, D. Brassard, J.-C. Kieffer, M. El Khakani, and F. Hegmann, Physical Review B **85**, 155120 (2012), ISSN 1098-0121, URL `http://link.aps.org/doi/10.1103/PhysRevB.85.155120`.

[21] Y. Muraoka and Z. Hiroi, Applied Physics Letters **80**, 583 (2002), ISSN 00036951, URL `http://link.aip.org/link/APPLAB/v80/i4/p583/s1&Agg=doi`.

[22] P. Scherrer, Nachr. Ges. Wiss. G\"{o}ttingen, Math.-Phys. Kl. **26**, 98 (1918).

[23] N. B. Aetukuri, A. X. Gray, M. Drouard, M. Cossale, L. Gao, A. H. Reid, R. Kukreja, H. Ohldag, C. a. Jenkins, E. Arenholz, et al., Nature Physics **9**, 661 (2013), ISSN 1745-2473, URL `http://www.nature.com/doifinder/10.1038/nphys2733`.

[24] R. A. Aliev, V. N. Andreev, V. M. Kapralova, V. A. Klimov, A. I. Sobolev, and E. B. Shadrin, Physics of the Solid State **48**, 929 (2006), ISSN 1063-7834, URL `http://link.springer.com/10.1134/S1063783406050180`.

[25] I. Khakhaev, F. A. Chudnovskii, and E. B. Shadrin, Physics of the Solid State **36**, 898 (1994), URL `http://adsabs.harvard.edu/abs/1994PhSS...36..898K`.

[26] J. Y. Suh, R. Lopez, L. C. Feldman, and R. F. Haglund, Journal of Applied Physics **96**, 1209 (2004), ISSN 00218979, URL `http://scitation.aip.org/content/aip/journal/jap/96/2/10.1063/1.1762995`.

[27] L. C. o. W. Wang, Mary), I. C. o. W. Novikova, Mary), J. M. Klopf, S. Madaras, G. P. Williams, E. Madaras, J. Lu, S. A. Wolf, et al., Advanced Optical Materials (2013), URL `http://onlinelibrary.wiley.com/doi/10.1002/adom.201300333/full`.

[28] M. Schubert, Physical review. B, Condensed matter **53**, 4265 (1996), ISSN 0163-1829, URL `http://www.ncbi.nlm.nih.gov/pubmed/9983979`.

[29] J. Lappalainen, S. Heinilehto, S. Saukko, V. Lantto, and H. Jantunen, Sensors and Actuators A: Physical **142**, 250 (2008), ISSN 09244247, URL `http://linkinghub.elsevier.com/retrieve/pii/S0924424707003780`.

[30] B. Wang, S. Chen, Z. Huang, and M. Fu, Applied Surface Science **258**, 5319 (2012), ISSN 01694332, URL `http://linkinghub.elsevier.com/retrieve/pii/S0169433212001882`.

[31] C. G. Granqvist, Solar Energy Materials and Solar Cells **91**, 1529 (2007), ISSN 09270248, URL `http://dx.doi.org/10.1016/j.solmat.2007.04.031`.

[32] T. D. Manning and I. P. Parkin, Journal of Materials Chemistry **14**, 2554 (2004), ISSN 0959-9428, URL `http://pubs.rsc.org/en/content/articlehtml/2004/jm/b403576n`.

[33] T. Driscoll, H.-T. Kim, B.-G. Chae, M. Di Ventra, and D. N. Basov,

Applied Physics Letters **95**, 043503 (2009), ISSN 00036951, URL `http://link.aip.org/link/?APPLAB/95/043503/1`.

[34] H.-T. Kim, B.-G. Chae, D.-H. Youn, S.-L. Maeng, G. Kim, K.-Y. Kang, and Y.-S. Lim, New Journal of Physics **6**, 52 (2004), ISSN 1367-2630, URL `http://iopscience.iop.org/article/10.1088/1367-2630/6/1/052`.

[35] A. Cavalleri, C. Tóth, C. Siders, J. A. Squier, F. Ráksi, P. Forget, and J. C. Kieffer, Physical Review Letters **87**, 237401 (2001), ISSN 0031-9007, URL `http://link.aps.org/doi/10.1103/PhysRevLett.87.237401`.

[36] M. Först, C. Manzoni, S. Kaiser, Y. Tomioka, Y. Tokura, R. Merlin, and a. Cavalleri, Nature Physics **7**, 854 (2011), ISSN 1745-2473, URL `http://www.nature.com/doifinder/10.1038/nphys2055`.

[37] A. Pashkin, C. Kübler, H. Ehrke, R. Lopez, A. Halabica, R. Haglund, R. Huber, and A. Leitenstorfer, Physical Review B **83**, 195120 (2011), ISSN 1098-0121, URL `http://link.aps.org/doi/10.1103/PhysRevB.83.195120`.

[38] K. G. West, J. Lu, L. He, D. Kirkwood, W. Chen, T. P. Adl, M. S. Osofsky, S. B. Qadri, R. Hull, and S. a. Wolf, Journal of Superconductivity and Novel Magnetism **21**, 87 (2008), ISSN 1557-1939, URL `http://link.springer.com/10.1007/s10948-007-0303-y`.

[39] P. Schilbe, Physica B **317**, 600 (2002).

[40] M. Pan, J. Liu, H. Zhong, S. Wang, Z.-f. Li, X. Chen, and W. Lu, Journal of Crystal Growth **268**, 178 (2004), ISSN 00220248, URL `http://linkinghub.elsevier.com/retrieve/pii/S0022024804005585`.

[41] X.-B. Chen, Journal of the Korean Physical Society **58**, 100 (2011), ISSN ISSN 0374-4884, URL `http://inis.iaea.org/Search/search.aspx?orig_q=RN:43045741`.

[42] K. Appavoo, D. Y. Lei, Y. Sonnefraud, B. Wang, S. T. Pantelides, S. a. Maier, and R. F. Haglund, Nano letters **12**, 780 (2012), ISSN 1530-6992, URL `http://www.ncbi.nlm.nih.gov/pubmed/22273268`.

[43] K. Sokolowski-Tinten, A. Cavalleri, and D. V. D. Linde, Applied Physics A **69**, 577 (1999).

[44] G. Gopalakrishnan, D. Ruzmetov, and S. Ramanathan, Journal of Materials Science **44**, 5345 (2009), ISSN 0022-2461, URL `http://www.springerlink.com/index/10.1007/s10853-009-3442-7`.

[45] E. Radue, E. Crisman, L. Wang, S. Kittiwatanakul, J. Lu, S. A. Wolf, R. Wincheski, R. A. Lukaszew, and I. Novikova, Journal of Applied Physics **113**, 233104 (2013).

[46] Z. Tao, T.-R. Han, S. Mahanti, P. Duxbury, F. Yuan, C.-Y. Ruan, K. Wang, and J. Wu, Physical Review Letters **109**, 1 (2012), ISSN 0031-9007, URL `http://link.aps.org/doi/10.1103/PhysRevLett.109.166406`.

[47] C. Kübler, H. Ehrke, R. Huber, R. Lopez, a. Halabica, R. Haglund, and a. Leitenstorfer, Physical Review Letters **99**, 116401 (2007), ISSN 0031-9007, URL `http://link.aps.org/doi/10.1103/PhysRevLett.99.116401`.

[48] K. Okazaki, H. Wadati, A. Fujimori, and M. Onoda, Physical Review B **69**, 1 (2004), `0312112`, URL `http://prb.aps.org/abstract/PRB/v69/i16/e165104`.

[49] L. Wang, E. Radue, S. Kittiwatanakul, C. Clavero, J. Lu, S. A. Wolf, I. Novikova, and R. A. Lukaszew, Optics letters **37**, 4335 (2012), ISSN 1539-4794, URL `http://www.ncbi.nlm.nih.gov/pubmed/23073454`.

[50] M. Seo, J. Kyoung, H. Park, S. Koo, H.-s. Kim, H. Bernien, B. J. Kim, J. H. Choe, Y. H. Ahn, H.-T. Kim, et al., Nano letters **10**, 2064 (2010), ISSN 1530-6992, URL `http://www.ncbi.nlm.nih.gov/pubmed/20469898`.

[51] A. Tselev, I. A. Luk'yanchuk, I. N. Ivanov, J. D. Budai, J. Z. Tischler, E. Strelcov, A. Kolmakov, and S. V. Kalinin, Nano letters **10**, 4409 (2010), ISSN 1530-6992, URL `http://www.ncbi.nlm.nih.gov/pubmed/20939599`.

[52] T. Kikuzuki, R. Takahashi, and M. Lippmaa, Physical Review B **82**, 144113 (2010), ISSN 1098-0121, URL `http://link.aps.org/doi/10.1103/PhysRevB.82.144113`.

[53] K. G. West, J. Lu, J. Yu, D. Kirkwood, W. Chen, Y. Pei, J. Claassen, and S. a. Wolf, Journal of Vacuum Science & Technology A: Vacuum, Surfaces, and Films **26**, 133 (2008), ISSN 07342101, URL `http://link.aip.org/link/JVTAD6/v26/i1/p133/s1&Agg=doi` `http://scitation.aip.org/content/avs/journal/jvsta/26/1/10.1116/1.2819268`.

[54] D. Brassard, S. Fourmaux, M. Jean-Jacques, J. C. Kieffer, and M. a. El Khakani, Applied Physics Letters **87**, 051910 (2005), ISSN 00036951, URL `http://link.aip.org/link/APPLAB/v87/i5/p051910/s1&Agg=doi`.

[55] M. M. Qazilbash, K. S. Burch, D. Whisler, D. Shrekenhamer, B. G. Chae, H. T. Kim, and D. N. Basov, Physical Review B **74**, 1 (2006), ISSN 1098-0121, URL `http://link.aps.org/doi/10.1103/PhysRevB.74.205118`.

[56] M. K. Liu, M. Wagner, E. Abreu, S. Kittiwatanakul, A. McLeod, Z. Fei, M. Goldflam, S. Dai, M. M. Fogler, J. Lu, et al., Physical Review Letters **111**, 1 (2013), ISSN 0031-9007, URL `http://link.aps.org/doi/10.1103/PhysRevLett.111.096602`.

[57] E. Abreu, S. Wang, G. Ramirez, and M. Liu, arXiv preprint arXiv: ... (2014), `arXiv:1410.6804v1`, URL `http://arxiv.org/abs/1410.6804`.

[58] S. Biermann, A. Poteryaev, A. I. Lichtenstein, and A. Georges, Physical Review Letters **94**, 026404 (2005), ISSN 0031-9007, `0410005v1`, URL `http://link.aps.org/doi/10.1103/PhysRevLett.94.026404`.

[59] T. L. Cocker, L. V. Titova, S. Fourmaux, H. C. Bandulet, D. Brassard, J. C. Kieffer, M. a. El Khakani, and F. a. Hegmann, Applied Physics Letters **97**, 221905 (2010), ISSN 00036951, URL `http://link.aip.org/link/APPLAB/v97/i22/p221905/s1&Agg=doi`.

[60] C. Berglund and H. Guggenheim, Physical Review **185**, 1022 (1969), URL `http://prola.aps.org/abstract/PR/v185/i3/p1022_1` `http://journals.aps.org/pr/abstract/10.1103/PhysRev.185.1022`.

[61] M. M. Qazilbash, M. Brehm, B.-G. Chae, P.-C. Ho, G. O. Andreev, B.-J. Kim, S. J. Yun, A. V. Balatsky, M. B. Maple, F. Keilmann, et al., Science **318**, 1750 (2007), ISSN 1095-9203, URL `http://www.ncbi.nlm.nih.gov/pubmed/18079396`.

[62] L. Wang, I. Novikova, J. M. Klopf, S. Madaras, G. P. Williams, E. Madaras, J. Lu, S. a. Wolf, and R. a. Lukaszew, Advanced Optical Materials **2**, 30 (2014), ISSN 21951071, URL `http://doi.wiley.com/10.1002/adom.201300333`.

[63] H. T. Kim, Y. W. Lee, B. J. Kim, B. G. Chae, S. J. Yun, K. Y. Kang, K. J. Han, K. J. Yee, and Y. S. Lim, Physical Review Letters **97**, 10 (2006), ISSN 00319007, `0608085`.

[64] M. Rini, Z. Hao, R. W. Schoenlein, C. Giannetti, F. Parmigiani, S. Fourmaux, J. C. Kieffer, a. Fujimori, M. Onoda, S. Wall, et al.,

Applied Physics Letters **92**, 181904 (2008), ISSN 00036951, URL `http://link.aip.org/link/APPLAB/v92/i18/p181904/s1&Agg=doi`.

[65] E. Abreu, M. Liu, J. Lu, K. G. West, S. Kittiwatanakul, W. Yin, S. a. Wolf, and R. D. Averitt, New Journal of Physics **14**, 083026 (2012), ISSN 1367-2630, URL `http://stacks.iop.org/1367-2630/14/i=8/a=083026?key=crossref.667002eceb37a540885b`

[66] S. Wall, L. Foglia, D. Wegkamp, K. Appavoo, J. Nag, R. F. Haglund, J. Stähler, and M. Wolf, Physical Review B **87**, 1 (2013), ISSN 1098-0121, URL `http://link.aps.org/doi/10.1103/PhysRevB.87.115126`.

[67] E. Radue, L. Wang, S. Kittiwatanakul, J. Lu, S. a. Wolf, E. Rossi, R. a. Lukaszew, and I. Novikova, Journal of Optics **17**, 025503 (2015), ISSN 2040-8978, URL `http://stacks.iop.org/2040-8986/17/i=2/a=025503?key=crossref.402967563bdc6925fc11`

[68] S. Lysenko, V. Vikhnin, F. Fernandez, a. Rua, and H. Liu, Physical Review B **75**, 075109 (2007), ISSN 1098-0121, URL `http://link.aps.org/doi/10.1103/PhysRevB.75.075109`.

[69] D. A. G. Bruggeman, Annalen der Physik **416**, 636 (1935), ISSN 00033804, URL `http://doi.wiley.com/10.1002/andp.19354160705`.

[70] R. Landauer, Journal of Applied Physics **23**, 779 (1952), ISSN 00218979.

[71] X. C. Zeng, D. J. Bergman, P. M. Hui, and D. Stroud, Physical Review B **38**, 10970 (1988), ISSN 01631829.

[72] E. Rossi, S. Adam, and S. Das Sarma, Physical Review B - Condensed Matter and Materials Physics **79**, 1 (2009), ISSN 10980121, `0809.1425`.

[73] J. Kana Kana, J. Ndjaka, G. Vignaud, a. Gibaud, and M. Maaza, Optics Communications **284**, 807 (2011), ISSN 00304018, URL `http://linkinghub.elsevier.com/retrieve/pii/S0030401810010874`.

[74] C. G. Granqvist and R. a. Buhrman, Journal of Applied Physics **47**, 2200 (1976).

[75] M. E. Fisher and A. N. Berker, Physical Review B **26**, 2507 (1982), ISSN 01631829.

[76] M. S. S. Challa, D. P. Landau, and K. Binder, Physical Review B **34**, 1841 (1986), ISSN 01631829.

[77] M. Zhang, M. Y. Efremov, F. Schiettekatte, E. A. Olson, A. T. Kwan, S. L. Lai, T. Wisleder, J. E. Greene, and L. H. Allen, Physical Review B - Condensed Matter and Materials Physics **62**, 10548 (2000), ISSN 01631829.

[78] Q. Jiang, J. C. Li, and B. Q. Chi, Chemical Physics Letters **366**, 551 (2002), ISSN 00092614.

[79] P. L. Kapitza, J. Phys. USSR **4** (1941).

[80] G. L. Pollack, Reviews of Modern Physics **41**, 48 (1969).

[81] R. Stoner and H. Maris, Physical review. B, Condensed matter **48**, 16373 (1993), ISSN 0163-1829, URL `http://www.ncbi.nlm.nih.gov/pubmed/10008218`.

[82] H. Wen, L. Guo, E. Barnes, J. H. Lee, D. a. Walko, R. D. Schaller, J. a. Moyer, R. Misra, Y. Li, E. M. Dufresne, et al., Physical Review B **88**, 165424 (2013), ISSN 1098-0121, URL `http://link.aps.org/doi/10.1103/PhysRevB.88.165424`.

[83] D. W. Oh, C. Ko, S. Ramanathan, and D. G. Cahill, Applied Physics Letters **96**, 0 (2010), ISSN 00036951.

[84] D. De Ligny, P. Richet, E. F. Westrum, and J. Roux, Physics and Chemistry of Minerals **29**, 267 (2002), ISSN 03421791.

[85] W. R. Thurber and A. J. H. Mante, Phys. Rev. **139**, A1655 (1965), URL `http://link.aps.org/doi/10.1103/PhysRev.139.A1655`.

[86] V. Pishchik, L. a. Lytvynov, and E. R. Dobrovinskaya, *Sapphire: Material, Manufacturing, Applications* (Springer US, 2009), 1st ed., ISBN 978-0-387-85694-0, URL `http://link.springer.com/10.1007/978-0-387-85695-7`.

[87] D. Wegkamp, M. Herzog, L. Xian, M. Gatti, P. Cudazzo, C. L. McGahan, R. E. Marvel, R. F. Haglund, A. Rubio, M. Wolf, et al., Physical Review Letters **113**, 216401 (2014), ISSN 0031-9007, URL `http://link.aps.org/doi/10.1103/PhysRevLett.113.216401`.

[88] S. Kittiwatanakul, J. Lu, and S. a. Wolf, Applied Physics Express **4**, 091104 (2011), ISSN 1882-0778, URL `http://stacks.iop.org/1882-0786/4/091104`.

[89] A. X. Gray, J. Jeong, N. P. Aetukuri, P. Granitzka, Z. Chen, R. Kukreja, and D. Higley, arXiv preprint arXiv: ... (2015).

[90] M. Först, R. Mankowsky, H. Bromberger, D. Fritz, H. Lemke, D. Zhu, M. Chollet, Y. Tomioka, Y. Tokura, R. Merlin, et al., Solid State Communications **169**, 24 (2013), ISSN 00381098, URL `http://linkinghub.elsevier.com/retrieve/pii/S0038109813002901`.

VITA

Elizabeth Radue

Elizabeth Radue was born in 1987 in the District of Columbia, and grew up in Mount Airy, MD. As a young girl she dreamed of being a writer/astronaut/ballerina/scientist/dolphin trainer; she figures one out of five isn't bad. She attended Sandy Spring Friends School from 1992-2005. She graduated from Mount Holyoke College cum laude in 2009 with a B.A. in physics. She entered College of William and Mary in Williamsburg, Virginia in Fall 2010 and joined Irina Novikova's group in the summer of 2011. She has worked on the vanadium dioxide project in collaboration with Ale Lukaszew's group.